Global Dirac optical potentials for elastic proton scattering from heavy nuclei

S. Hama and B. C. Clark
Department of Physics, The Ohio State University, Columbus, Ohio 43210

E. D. Cooper*
Department of Physics, McGill University, Montreal, Quebec, Canada H3A 2T8
and Department of Physics, Surrey University, Guildford GU2 5XH, Surrey, England

H. S. Sherif
Department of Physics, University of Alberta, Alberta, Canada T6G 2J1

R. L. Mercer
IBM Thomas J. Watson Research Center, Yorktown Heights, New York 10598
(Received 29 September 1989)

We present global Dirac optical model fits to elastic proton scattering data from heavy nuclear targets at energies between 65 and 1040 MeV. Such optical potentials provide critical input for a wide variety of nuclear reactions. The energy and mass number dependence of the parameters in the Lorentz four-vector and scalar potentials of Dirac phenomenology are given. The characteristic features of the potentials are discussed and the predictive power of the global approach presented here is tested for both interpolation and extrapolation.

I. INTRODUCTION

There is considerable interest in relativistic treatments of nuclear reactions such as $(e,e'p)$, (p,p'), $(p,2p)$, (p,π), and (γ,p). In these studies the Lorentz four-vector (timelike component only) and scalar optical potentials used in the Dirac equation are generally employed to obtain distorted waves for use in both relativistic and nonrelativistic DWBA calculations.[1-3] In addition, they can provide input to relativistic coupled channel treatments of inelastic nucleon-nucleus scattering.[4-7] This increased demand for relativistic optical model potentials has led to the development of global fitting approaches for treating elastic nucleon-nucleus scattering data over a wide range of energies.[8-10] These approaches have, however, considered only the energy dependence of the potential parameters. In this work we present a global optical potential treatment which includes both the energy (E) and mass number (A) dependence of the Dirac optical potential parameters. The model used is the standard Lorentz–scalar-Lorentz vector model of Dirac phenomenology which has been remarkably successful in reproducing a large body of elastic nucleon-nucleus elastic and inelastic scattering data over a wide range of projectile energies and target mass numbers.[1-16]

By way of introduction we review briefly the global treatments described in Refs. 8–10. The global potentials described in Refs. 11 and 12 were designed for specific purposes. In Ref. 11 the imaginary optical potential for ^{12}C was investigated between 200 and 300 MeV. The potentials given in Ref. 12 were used in $(p,2p)$ reaction calculation for ^{40}Ca and have a form similar to that described in Ref. 9.

In general, the scalar and vector optical potentials are written

$$V(r,E)=V_0(E)f_0(r,E) + i[W_0(E)g_0(r,E)+W_{0sp}(E)h_0(r,E)] , \quad (1)$$

$$S(r,E)=V_s(E)f_s(r,E) + i[W_s(E)g_s(r,E)+W_{ssp}(E)h_s(r,E)] . \quad (2)$$

The imaginary parts can contain both volume and surface terms. The real $f(r,E)$ and imaginary $g(r,E)$ volume form factors have, in a number of cases, been taken to be symmetrized Woods-Saxon (SWS's) and the surface form factors $h(r,E)$ are taken as the derivative of a SWS with, of course, the possibility of different geometry parameters. The surface terms were included in order to extend the model to low energies. For future reference we note that the effective central and spin-orbit potentials arising in the second-order Dirac equation given by

$$[\nabla^2+(E-V_c)^2-m^2-2E(U_{\rm cent}+U_{\rm s.o.}\sigma\cdot\mathbf{L})]\psi(\mathbf{r})=0 \quad (3)$$

are written[13]

$$U_{\rm cent}=\frac{1}{2E}(2EV+2mS-V^2+S^2-2V_cV+2EU_D) , \quad (4)$$

$$U_D=\frac{1}{2E}\left[-\frac{1}{2r^2A}\frac{d}{dr}\left[r^2\frac{dA}{dr}\right]+\frac{3}{4A^2}\left[\frac{dA}{dr}\right]^2\right] , \quad (5)$$

$$U_{\rm s.o.}=\frac{1}{2E}\left[-\frac{1}{rA}\left[\frac{dA}{dr}\right]\right] , \quad (6)$$

and where

$$A(r)=(m+S+E-V-V_c)/(m+E)\ . \tag{7}$$

The Coulomb potential is calculated from the empirical charge distribution of the target nucleus as tabulated in Vol. 37 of the Atomic and Nuclear Data Tables. We have checked the effect of replacing V_c by a uniformly charged sphere with the same rms radius and find the differences to be small; however, we encourage the use of the correct Coulomb potential.

The authors of Ref. 8 considered elastic $p+^{40}$Ca scattering data at energies above 150 MeV and employed four different assumptions regarding the energy dependence of the potential parameters as well as several forms for the volume form factors; no surface terms were included. The use of several models was made in order to provide a method for testing the effects of possible ambiguities in the potentials upon reaction calculations. In case one, the geometries of the real scalar and vector potentials were assumed to be energy independent with the parameters fixed by the method described in Ref. 16, which used a simplified one-boson exchange potential (OBEP) model of the *NN* potential to determine the potential parameters. In case two, the real optical potentials were constrained by relativistic Hartree considerations as described in Refs. 8 and 13. Thus, in both cases all of the energy dependence of the real optical potentials was contained in the strength parameters. For both cases the imaginary strengths and geometries, taken as SWS's, could have quadratic energy dependence. The other two cases considered in Ref. 8 were investigated under a more restrictive scenario in which both real and imaginary form factors, taken as SWS's, were assumed to be energy independent. In these two cases all of the energy dependence is embedded in the strength parameters. The authors of Ref. 8 achieved quite acceptable global fits to the elastic scattering data considered and the parameters exhibited good properties with respect to interpolation.

In Ref. 9 global Dirac optical potentials for $p+^{40}$Ca for the energy range 21–200 MeV were reported. In this energy region the imaginary part of the effective central potential changes from a volume to a surface peaked form. In order to accommodate this change, surface terms were added to the scalar and vector imaginary parts, and the energy dependence of these surface terms was assumed to be that of a decaying exponential. In Ref. 9 all of the energy dependence was assumed to be in strengths. The energy-independent geometries were searched on, and a common geometry was found for all energies considered. One interesting observation was that the following combinations of potential strengths are, in order of decreasing importance, relevant for fitting elastic data: V_v+V_s, W_v+W_s, V_v-V_s, and W_v-W_s.

In Ref. 10, a global analysis of intermediate energy nucleon $+^{208}$Pb scattering data has been performed simultaneously for both neutron and proton scattering data by including recently measured neutron total cross sections[17] in addition to proton elastic scattering data. Several different energy dependences were studied to construct best-fit nucleon-nucleus potentials for the energy interval of 95–300 MeV.

In this paper we give a global parametrization of the Dirac optical model potential whose parameters are functions of both energy and target mass number. We believe these global optical models have the most extensive range of E and A to date; regardless of whether the treatment is relativistic, as in this work, or nonrelativistic. Of course, the potentials obtained here can be used in nonrelativistic calculations by using the definitions of the effective central and spin-orbit potentials given in Eqs. (4) and (6). The data set consists of elastic proton scattering data for heavy nuclei from ^{40}Ca to ^{208}Pb in the energy range of 65–1040 MeV.

The organization of the paper is as follows. In Sec. II, we describe the two models employed in the analysis and the experimental data set used. The parametrization of the global optical potentials with respect to their E and A dependence is presented. The results of the global optical potential analysis are examined in Sec. III. This section discusses the quality of the typical fits to the data as well as the predictive power of the model with respect to both extrapolation and interpolation in E and A. An example of the use of both global potentials in inelastic $p+A$ scattering is given in Sec. IV. Section V includes a summary of the conclusions, and plans for the future extensions of this work.

II. THE OPTICAL POTENTIAL MODELS

This work employs the standard Lorentz scalar-vector optical potential model of Dirac phenomenology.[8–16] GRUMBLE, a modified version of the Dirac partial wave program RUNT,[18] is used in the analysis. Independent checks of the results are made using the Dirac coupled channel program SENITH.[19] Using these completely independent programs gives us confidence in the numerical work. Both of these programs have been used in the analysis of nucleon-nucleus elastic scattering data for wide range of projectile energies and target mass numbers.

Now we discuss the two parametrizations for the global optical potentials used in this work. As we cover a large range in A, and plan to consider an even larger range, it is desirable to take into account recoil effects. This we do using the Cooper-Jennings procedure described in Ref. 20. This procedure has the appealing feature of just requiring that the optical potentials be multiplied by factors depending on the invariant, $\sqrt{s}$, the total c.m. energy of the p-A system. Two Cooper-Jennings recoil factors, one for the Lorentz scalar potential and one for the Lorentz vector potential, are defined as follows:

$$R_v=\frac{E_T}{\sqrt{s}} \tag{8}$$

and

$$R_s=\frac{W_T}{\sqrt{s}}\ . \tag{9}$$

Here E_T is the total c.m. energy of the target nucleus and W_T the mass of the target nucleus.

A simple extension of the optical potentials described

in Ref. 9 is described first. For the vector potentials we write

$$V_v(r,E,A)=R_v(V_0+V_1/E+V_2/E^2+V_3/E^3)\times f(r,R_1,z_1) \quad (10)$$

and

$$W_v(r,E,A)=R_v(W_0+W_1/E+W_2/E^2+W_3/E^3)\times f(r,R_2,z_2)+R_v W_{sp}\times\exp(-\lambda E)z_3\frac{d}{dR_3}f(r,R_3,z_3) \quad (11)$$

and the scalar potential has the same form, with vector parameters and the Cooper-Jennings recoil factor replaced by their scalar counterparts. In Eqs. (10) and (11), E is the total energy of the incident proton in the c.m. frame in MeV divided by 1000 MeV. The volume form factors $f(r,E,z)$ are SWS's given by

$$f(r,R,z)=\{1+\exp[(r-R)/z]\}^{-1}\times\{1+\exp[-(r+R)/z]\}^{-1} . \quad (12)$$

The geometry parameters R_i and z_i have E and A dependence given by

$$R_i=A^{1/3}(r_{0i}+r_{1i}/A+r_{2i}/A^2+r_{3i}/E+r_{4i}/E^2+r_{5i}/E^3) \quad (13)$$

and

$$z_i=a_{0i}+a_{1i}/A+a_{2i}/A^2+a_{3i}/E+a_{4i}/E^2+a_{5i}/E^3 , \quad (14)$$

where $i=1$, 2, and 3 and the extension to the scalar potentials is clear. The surface term geometry parameters are assumed to be independent of E so that R_3 and z_3 are functions of A only. The results obtained from this parametrization described are denoted as fit 1.

At the conclusion of our work using fit 1 we observed that the volume integral per nucleon of the real and imaginary scalar and vector potentials at a given energy were almost independent of A. To order (z^2) the volume integral of the form factors given by Eq. (12) is

$$(4/3)\pi R(R^2+\pi^2 z^2) , \quad (15)$$

and is, for fit 1, approximately proportional to A. When the diffuseness parameter z is taken to be a quadratic function of A, the radius parameter R may be written as

$$A^{1/3}(a_0+a_1A^{-2/3}+a_2A^{1/3}) .$$

Using this observation we write the second parametrization for the vector potentials as

$$V_v(r,E,A)=R_v(V_0+V_1/E+V_2/E^2+V_3/E^3)\times f(r,R_1,z_1) \quad (16)$$

and

$$W_v(r,E,A)=R_v(W_0+W_1/E+W_2/E^2+W_3/E^3)\times f(r,R_2,z_2)+R_v(W_{0sp}+W_{1sp}/E+W_{2sp}/E^2+W_{3sp}/E^3)z_3\frac{d}{dR_3}f(r,R_3,z_3) . \quad (17)$$

The geometry parameters R_i and z_i are given by

$$R_i=A^{1/3}(r_{0i}+r_{1i}A^{-2/3}+r_{2i}A^{1/3}+r_{3i}/E+r_{4i}/E^2+r_{5i}/E^3) , \quad (18)$$

$$z_i=a_{0i}+a_{1i}A+a_{2i}A^2+a_{3i}/E+a_{4i}/E^2+a_{5i}/E^3 , \quad (19)$$

where $i=1$, 2, and 3 and, as in fit 1, R_3 and z_3 are assumed to be independent of E. The scalar potentials are defined in the same way. This second parametrization is denoted as fit 2.

III. ANALYSES AND RESULTS

In this section we describe the two global analyses which use the optical potentials discussed above. We discuss the characteristic features of the Lorentz scalar and vector potentials obtained, as well as those of the effective central and spin-orbit potentials given by Eqs. (4) and (6), respectively. However, as the data sets considered, and the treatment of those data sets is of paramount importance in any global treatment of experimental data, we turn now to a discussion of them.

The experimental data sets used in the global optical potential search are given in Table I along with the references for them. Nonlocalities in the optical potential and/or channel coupling effects are presumably important at larger angles. Therefore we restrict the data sets to those angles smaller than $90°_{c.m.}$ or angles corresponding to momentum transfer 3 fm^{-1}, whichever is smaller. To allow for possible systematic errors we changed the cross section errors by adding 3% of the cross section in quadrature with the quoted experimental errors to form the final cross section errors, $\Delta\sigma$. For the spin observables A_y and Q, we added 0.02 in quadrature to the experimental errors given for these observables to form the final errors ΔA_y and ΔQ. In addition, in order to weight the various observables as well as the various data sets in a manner which, at least approximately, gives them roughly equal standing, in the least-squares sense, we multiplied the χ^2's by the weighting factors given in Table I. The total χ^2 minimized during the search is given by

$$\chi_T^2=\sum_{j=1}^{N}[\chi^2_{\sigma_j}(j)+\chi^2_{A_y}(j)+\chi^2_Q(j)] , \quad (20)$$

TABLE I. Listed are the experimental data sets used in the global searches. The total χ^2 per degree of freedom for fits 1 is 8.37 and that of fit 2 is 8.24.

Target	T_p (MeV)	N_σ	N_{A_y}	N_Q	ω_σ	ω_{A_y}	ω_Q	F_N Fit 1/Fit 2	Reference
^{40}Ca	65.0	30	30	0	0.7	0.5	0.2	1.0888/1.0608	21
	80.0	42	22	0	0.7	0.5	0.2	0.9620/0.9519	22,23
	135.0	33	0	0	0.9	0.7	0.2	1.0032/0.9845	23
	160.0	32	16	0	0.9	0.7	0.2	0.9392/0.9186	22,23
	181.3	29	29	0	0.9	0.7	0.2	0.9580/0.9352	22,23
	200.0	93	93	12	0.9	0.7	0.2	1.0024/0.9702	24
	300.0	90	90	0	0.9	0.7	0.2	1.0710/1.0443	25
	400.0	56	56	0	0.9	0.7	0.2	1.0617/1.0440	25
	497.5	154	156	32	0.9	0.7	0.2	1.0062/1.0028	26,27
	613.0	138	0.	0	0.9	0.7	0.2	1.0886/1.1010	29
	797.5	113	118	30	0.9	0.7	0.2	1.0158/1.0333	30,31,32
	1040.0	61	24	0	0.9	0.7	0.2	1.0188/1.0209	33
^{48}Ca	65.0	23	23	0	0.7	0.5	0.2	1.0163/1.0009	21
	497.5	126	142	0	0.9	0.7	0.2	0.9512/0.9194	26
	797.5	75	69.	0	0.9	0.7	0.2	0.8980/0.8566	30
	1044.0	60	0	0	0.9	0.7	0.2	0.8916/0.8118	33
^{56}Fe	65.0	28	28	0	0.7	0.5	0.2	1.0295/1.0107	21
^{60}Ni	65.0	30	30	0	0.7	0.5	0.2	0.9419/0.9271	21
^{90}Zr	65.0	26	24	0	0.7	0.5	0.2	1.0687/1.0561	21
	80.0	59	24	0	0.7	0.5	0.2	0.9247/0.9473	22,23
	135.0	71	0	0	0.9	0.7	0.2	0.9340/0.9639	23
	160.0	42	27	0	0.9	0.7	0.2	0.8592/0.8685	22,23
	182.0	32	0	0	0.9	0.7	0.2	0.9686/0.9618	23
	500.0	147	158	0	0.9	0.7	0.2	0.9604/0.9611	26
	800.0	131	129	0.	0.9	0.7	0.2	1.0885/1.0637	34
^{208}Pb	65.0	51	51	0	0.7	0.5	0.2	0.9684/0.9391	21
	80.0	56	0	0	0.7	0.5	0.2	0.9986/1.0102	23
	121.0	67	0	0	0.9	0.7	0.2	0.9693/0.9864	23
	160.0	59	30	0	0.9	0.7	0.2	1.0328/1.0306	22,23
	182.0	37	47	0	0.9	0.7	0.2	0.9714/0.9653	22,23
	200.0	99	100	0	0.9	0.7	0.2	0.9291/0.9250	25
	400.0	143	143	0	0.9	0.7	0.2	1.0419/1.0387	35
	497.5	122	159	24	0.9	0.7	0.2	0.9570/0.9829	26,28
	797.5	194	108	29	0.9	0.7	0.2	0.9928/1.0042	32,34,36

where N is the total number of data sets in the search. The individual χ^2's are written for each data set j,

$$\chi^2_\sigma=\sum_{i=1}^{N_\sigma}\left[\frac{F_N\sigma_{\text{exp}}(i)-\sigma_{\text{calc}}(i)}{\omega_\sigma\Delta\sigma(i)}\right]^2, \tag{21a}$$

$$\chi^2_{A_y}=\sum_{i=1}^{N_{A_y}}\left[\frac{A_{y_{\text{exp}}}(i)-A_{y_{\text{calc}}}(i)}{\omega_{A_y}\Delta A_y(i)}\right]^2, \tag{21b}$$

and

$$\chi^2_Q=\sum_{i=1}^{N_Q}\left[\frac{Q_{\text{exp}}(i)-Q_{\text{calc}}(i)}{\omega_Q\Delta Q(i)}\right]^2, \tag{21c}$$

where ω_σ, ω_{A_y}, and ω_Q are the weighting factors for the jth data set and F_N is the normalization of the cross section for the jth data set given by

$$F_N=\frac{\sum_{i=1}^{N_\sigma}\{\sigma_{\text{calc}}(i)\sigma_{\text{exp}}(i)/[\Delta\sigma(i)]^2\}}{\sum_{i=1}^{N_\sigma}\{[\sigma_{\text{exp}}(i)]^2/[\Delta\sigma(i)]^2\}}. \tag{22}$$

F_N is searched on and the values are given in Table I. The data set used in the analysis contains 4602 data points.

The difference between the optical potentials used in fit

TABLE II. Global optical potential parameters for fit 1 as given in Eqs. (10)–(14). The strengths are given in MeV, the geometrical parameters are in fm, and λ is dimensionless. A computer program GLOBAL which produces tabulated scalar and vector potentials from these parameters is available from the authors. See Ref. 49. ($NE+n$ denotes $N\times 10^n$.)

	Vector (real)	Scalar (real)		Vector (imaginary)	Scalar (imaginary)
V_0	−0.593 711E +02	0.144 635E +03	W_0	−0.187 370E +03	0.767 390E +02
V_1	0.243 991E +03	−0.115 015E +04	W_1	0.261 183E +03	0.896 685E +02
V_2	0.422 820E +03	0.864 680E +03	W_2	−0.247 983E +03	−0.247 983E +03
V_3	−0.281 139E +03	−0.281 139E +03	W_3	0.127 567E +03	0.127 567E +03
r_{01}	0.164 460E +01	0.165 499E +01	r_{02}	0.731 599E +00	0.106 401E +01
r_{11}	−0.133 264E +02	−0.133 258E +02	r_{12}	−0.378 503E +01	−0.233 260E +01
r_{21}	0.334 714E +03	0.325 457E +03	r_{22}	0.710 760E +02	0.229 048E +02
r_{31}	−0.163 304E +01	−0.166 097E +01	r_{32}	0.159 654E +01	0.603 736E −01
r_{41}	0.169 182E +01	0.174 220E +01	r_{42}	−0.223 619E +01	0.537 633E −01
r_{51}	−0.505 995E +00	−0.545 308E +00	r_{52}	0.116 266E +01	0.680 720E −01
a_{01}	0.309 170E +01	0.211 241E +01	a_{02}	0.100 835E +01	0.646 036E +00
a_{11}	−0.942 102E +01	−0.785 078E +01	a_{12}	−0.326 173E +02	−0.406 376E +02
a_{21}	0.170 789E +03	0.133 156E +03	a_{22}	0.968 429E +03	0.132 273E +04
a_{31}	−0.996 093E +01	−0.603 129E +01	a_{32}	−0.870 205E +00	0.160 396E +00
a_{41}	0.140 240E +02	0.897 855E +01	a_{42}	0.101 693E +01	0.166 333E +00
a_{51}	−0.651 832E +01	−0.440 066E +01	a_{52}	−0.375 525E +00	−0.278 618E +00
			W_{sp}	0.391 326E +03	−0.778 311E +05
			λ	0.265 868E +01	0.726 225E +01
			r_{03}	0.109 691E +01	0.117 144E +01
			r_{13}	0.212 733E +02	0.445 545E +01
			r_{23}	−0.100 298E +04	−0.418 481E +03
			a_{03}	0.950 649E +00	0.840 840E +00
			a_{13}	−0.531 595E +02	−0.434 704E +02
			a_{23}	0.136 272E +04	0.131 545E +04

TABLE III. Global optical potentials parameters for fit 2 as given in Eqs. (16)–(19). The strengths are given in MeV and the geometry parameters in fm. A computer program GLOBAL which produces tabulated scalar and vector potentials from these parameters is available from the authors. See Ref. 49. ($NE+n$ denotes $N\times 10^n$.)

	Vector (real)	Scalar (real)		Vector (imaginary)	Scalar (imaginary)
V_0	0.162 663E +03	−0.786 320E +03	W_0	−0.949 660E +03	0.127 600E +04
V_1	−0.428 584E +03	0.215 619E +04	W_0	0.308 267E +04	−0.438 397E +04
V_2	0.959 310E +03	−0.281 098E +04	W_2	−0.374 717E +04	0.537 798E +04
V_3	−0.374 010E +03	0.103 025E +04	W_3	0.156 799E +04	−0.222 344E +04
r_{01}	0.118 178E +01	0.968 875E +00	r_{02}	0.228 599E +00	0.205 572E +01
r_{11}	−0.123 158E +00	−0.281 597E +00	r_{12}	0.332 582E +01	0.127 931E +01
r_{21}	0.234 456E −01	0.219 828E −01	r_{22}	0.528 099E −01	0.206 096E −01
r_{31}	−0.638 310E +00	0.227 499E +00	r_{32}	0.290 166E +01	−0.454 134E +01
r_{41}	0.514 879E +00	−0.527 801E +00	r_{42}	−0.453 304E +01	0.561 357E +01
r_{51}	−0.513 080E −01	0.346 211E +00	r_{52}	0.230 291E +01	−0.206 883E +01
a_{01}	0.367 009E +01	0.290 644E +01	a_{02}	0.189 637E +01	0.338 803E +00
a_{11}	0.900 712E −03	0.881 106E −03	a_{12}	−0.276 306E −02	−0.388 022E −02
a_{21}	−0.125 634E −05	−0.141 390E −05	a_{22}	0.131 470E −04	0.196 852E −04
a_{31}	−0.125 369E +02	−0.944 671E +01	a_{32}	−0.513 141E +01	0.219 169E +01
a_{41}	0.167 826E +02	0.128 925E +02	a_{42}	0.736 379E +01	−0.274 821E +01
a_{51}	−0.742 252E +01	−0.582 424E +01	a_{52}	−0.346 781E +01	0.114 420E +01
			W_{0sp}	0.665 325E +03	−0.392 815E +03
			W_{1sp}	−0.122 515E +04	0.887 654E +03
			W_{2sp}	0.661 619E +03	−0.558 651E +03
			W_{3sp}	−0.378 568E +02	0.100 805E +02
			r_{03}	0.817 165E +00	0.820 507E +00
			r_{13}	0.228 100E +01	0.211 267E +01
			r_{23}	0.481 430E −01	0.627 332E −01
			a_{03}	0.769 104E +00	0.970 102E +00
			a_{13}	−0.259 660E −02	−0.337 844E −02
			a_{23}	0.131 676E −04	0.155 953E −04

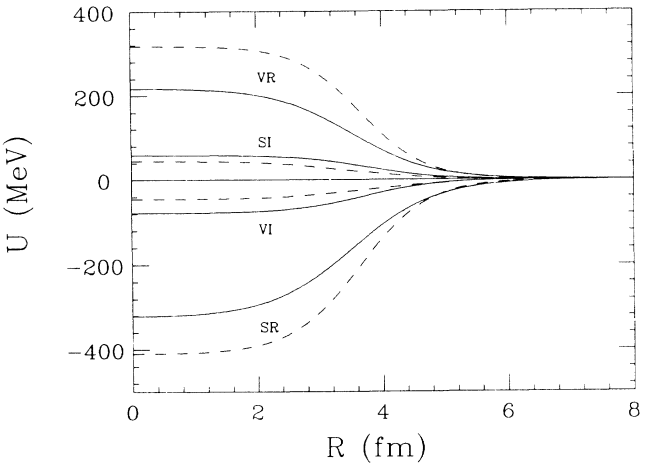

FIG. 1. The real scalar (SR) and imaginary scalar (SI), and the real vector (VR) and imaginary vector (VI) optical potentials for $p+^{40}$Ca from fit 1. The solid lines give the potentials at 497.5 MeV and the dashed lines give the potentials at 65 MeV.

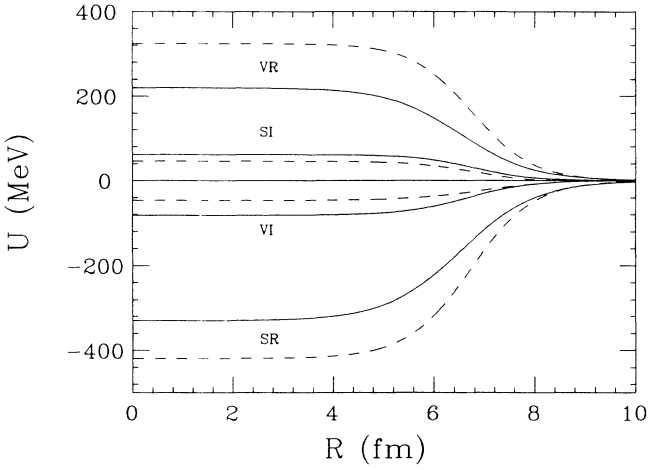

FIG. 3. The scalar, SR and SI, and vector, VR and VI, optical potentials for $p+^{208}$Pb from fit 1. The solid lines give the potentials at 497.5 MeV and the dashed lines give the potentials at 65 MeV.

1 given by Eqs. (10) and (11) and those of fit 2 given by Eqs. (16) and (17) is in the energy dependence of the strength of the imaginary surface term. In both cases the volume terms have polynomial energy dependence. However, the two fits treat the order of the polynomial included in the search differently. In fit 1, presented in Table II, cubic terms were retained for the combination V_v+V_s and W_v+W_s, quadratic terms for V_v-V_s, and linear terms for W_v-W_s. Including the geometry parameters and the energy-dependence parameter in the surface strength, there are a total of 77 parameters. For fit 2, the coefficients are given in Table III; all four combinations contained cubic terms, as did the surface terms. Fit 2 has a total of 84 parameters. As can be seen from the total χ^2 per degree of freedom given in Table I, the fits are of comparable quality and, in fact, both fit 1 and fit 2 represent the cross section and spin observable data quite well.

The scalar and vector global optical potentials for $p+^{40}$Ca and $p+^{208}$Pb are shown in Figs. 1–4 for two different incident proton energies, 65 and 497.5 MeV. The corresponding behavior of the imaginary surface terms, which are included in Figs. 1–4, are shown in Figs. 5–8. It is clear that the fit 1 parametrization has considerably less surface peaking than fit 2, and that in fit 2 the surface peaking persists to much higher energies.

In order to get some feeling for the relationship of these phenomenological potentials with potentials obtained from a more microscopic procedure, we show in Figs. 9 and 10 comparisons with the relativistic impulse approximation (RIA) calculations of Ref. 37 and well as the calculations of Murdock and Horowitz,[38] RIA-MH, which extend the RIA to include some exchange effects as well as an approximate treatment of Pauli blocking. In Fig. 9 we show the results for $p+^{40}$Ca at 497.5 MeV. Here the RIA works very well. Below 400 MeV the corrections included by Murdock and Horowitz become more important, and in Fig. 10 we show their results along with the standard RIA. At the lower energy it is

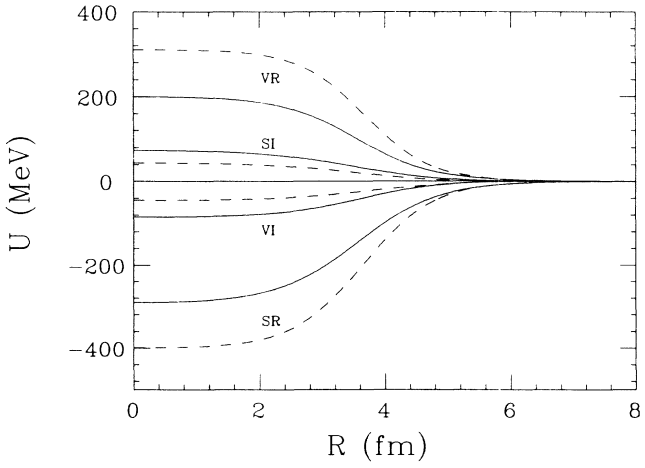

FIG. 2. The same as Fig. 1 except for fit 2.

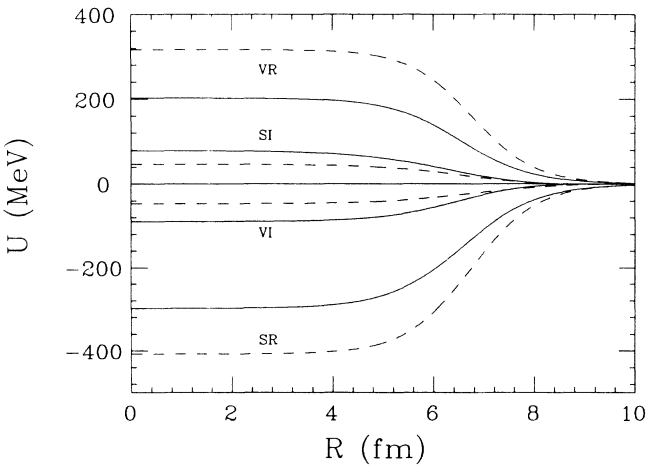

FIG. 4. The same as Fig. 3, except for fit 2.

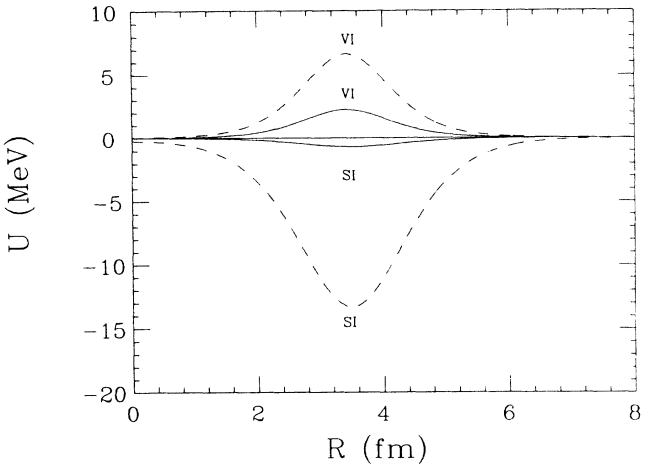

FIG. 5. The surface term optical potential for $p + {}^{40}$Ca from fit 1. The solid lines give the potentials at 497.5 MeV and the dashed lines give the potentials at 65 MeV.

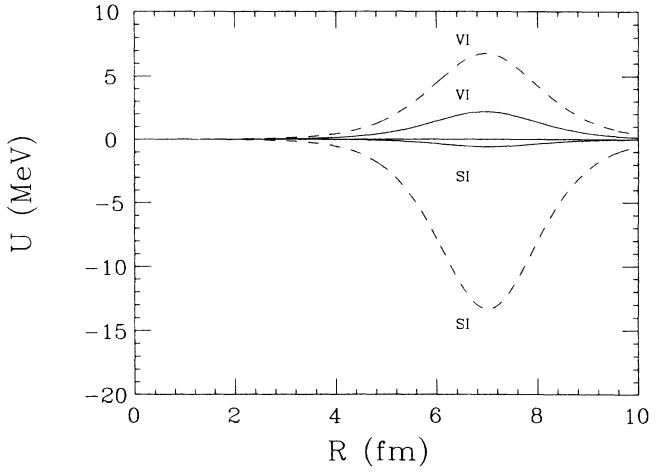

FIG. 7. The surface term optical potential for $p + {}^{208}$Pb from fit 1. The solid lines give the potentials at 497.5 MeV and the dashed lines give the potentials at 65 MeV.

clear that the optical potential produced by the uncorrected RIA does not agree with the phenomenological potential.

In Figs. 11–14 we show the typical quality of the agreement with data for several cases. All of the observables are well reproduced up to 3 fm^{-1} (corresponding to $32°_{\text{c.m.}}$ for 497.5 MeV $p + {}^{40}$Ca). Of course single-energy, single-A fits give lower χ^2's, but we feel that for a global parametrization which spans such a large range of E and A that the results are acceptable.

It is, of course, very important that the parametrization allows interpolation so that we can predict optical potentials for energies or targets not included in the data set. Interpolation in energy was done for $p + {}^{40}$Ca at 362 MeV, shown in Fig. 15, and in mass number for $p + {}^{124}$Sn at 795.5 MeV, shown in Fig. 16. In Fig. 15, we observe that both cross section and A_y are fairly well reproduced; however, the second and third minima in cross section are slightly shifted inward in angle in comparison with the data. As shown in Fig. 16, interpolation in A predicts an optical potential which gives a very good representation of both cross section and A_y data for ^{124}Sn at 795.5 MeV.

Finally we consider interpolation to an odd-A target. Consideration of targets which are deformed presents a particularly difficult problem as the scalar-vector (SV) model may not be appropriate. In spite of this, we considered the slightly deformed target ^{89}Y at 65 MeV and the results of this interpolation, shown in Fig. 17, are very good for this case; however, predictions for the cross sections (no A_y data are available) for the very deformed targets ^{154}Sm and ^{176}Yb at 800 MeV are not satisfactory, as shown in Fig. 18. Therefore, we would urge caution when using the global parameters for deformed nuclei.

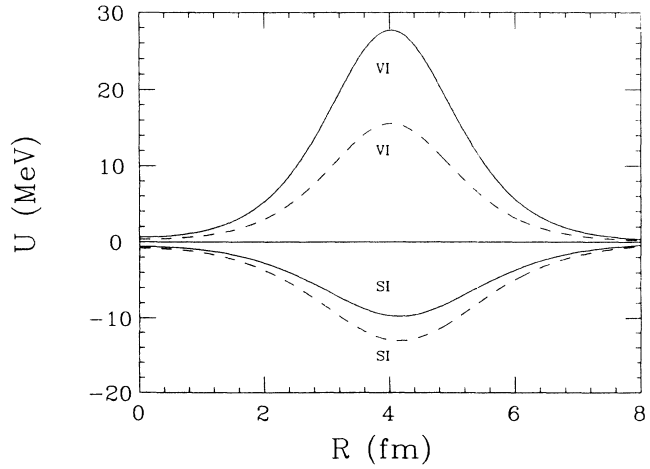

FIG. 6. The same as Fig. 5, except for fit 2.

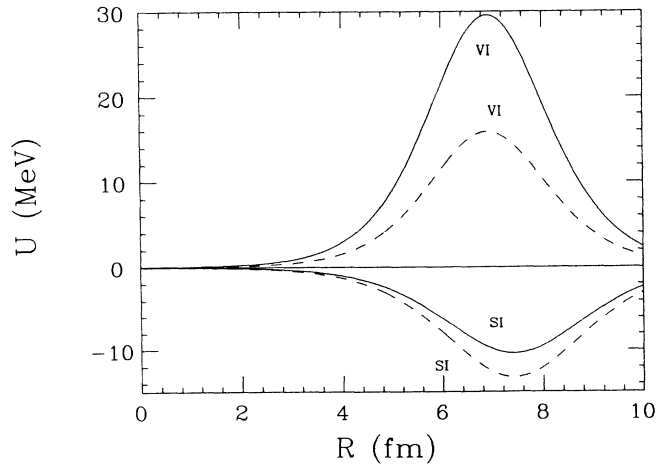

FIG. 8. The same as Fig. 7, except for fit 2.

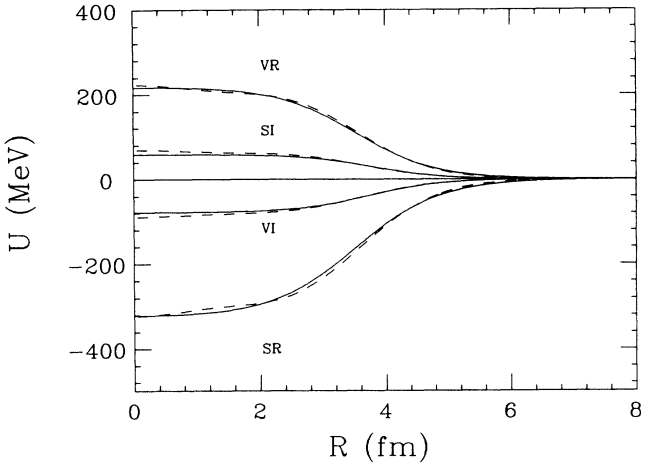

FIG. 9. Comparison of the scalar and vector potentials and 497.5 MeV for $p+{}^{40}$Ca from fit 1 with the RIA potentials. The solid lines give the phenomenological potentials and the dashed lines the RIA potentials.

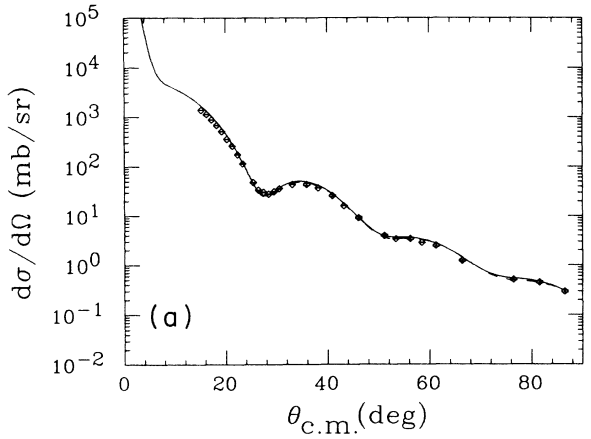

Global parametrizations have historically had great difficulties in predicting potentials outside the range covered by the data set. We examine this point next; extrapolations in both E and A are considered, separately and together. The parameters of both fit 1 and fit 2 are used in the calculations in order that we may see which set does the better job. For interpolation either fit was equally successful. The polynomial form of the energy dependence is known to cause problems when energies outside the range are considered; however, if the extrapolation is not too large, then the results appear to be reasonable. Consider, for example, $p+{}^{40}$Ca at 40 MeV which represents a sizable extrapolation from 65 MeV,

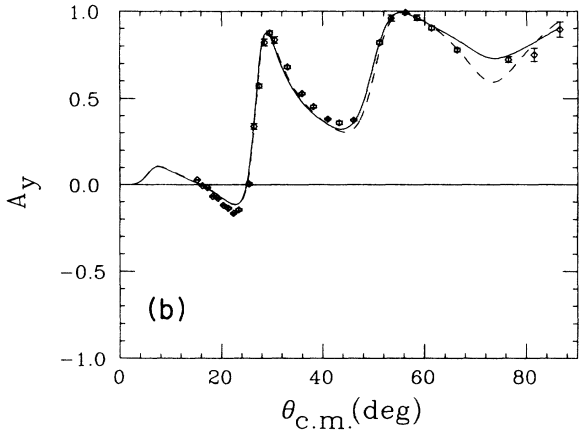

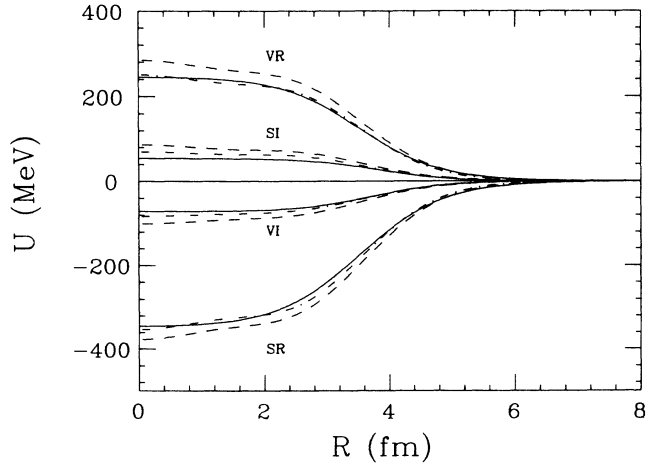

FIG. 10. The same as Fig. 9 except that the dashed-dotted line shows the RIA-MH potentials and the proton energy is 362 MeV.

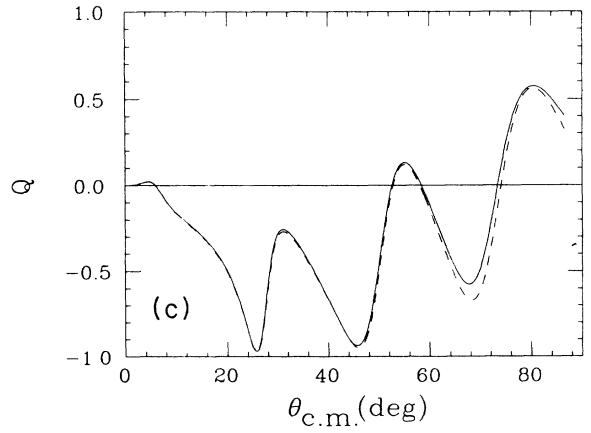

FIG. 11. Elastic scattering observables at 65 MeV for $p+{}^{40}$Ca calculated using the parameters of fits 1 (solid line) and 2 (dashed line). The experimental data are from Ref. 21.

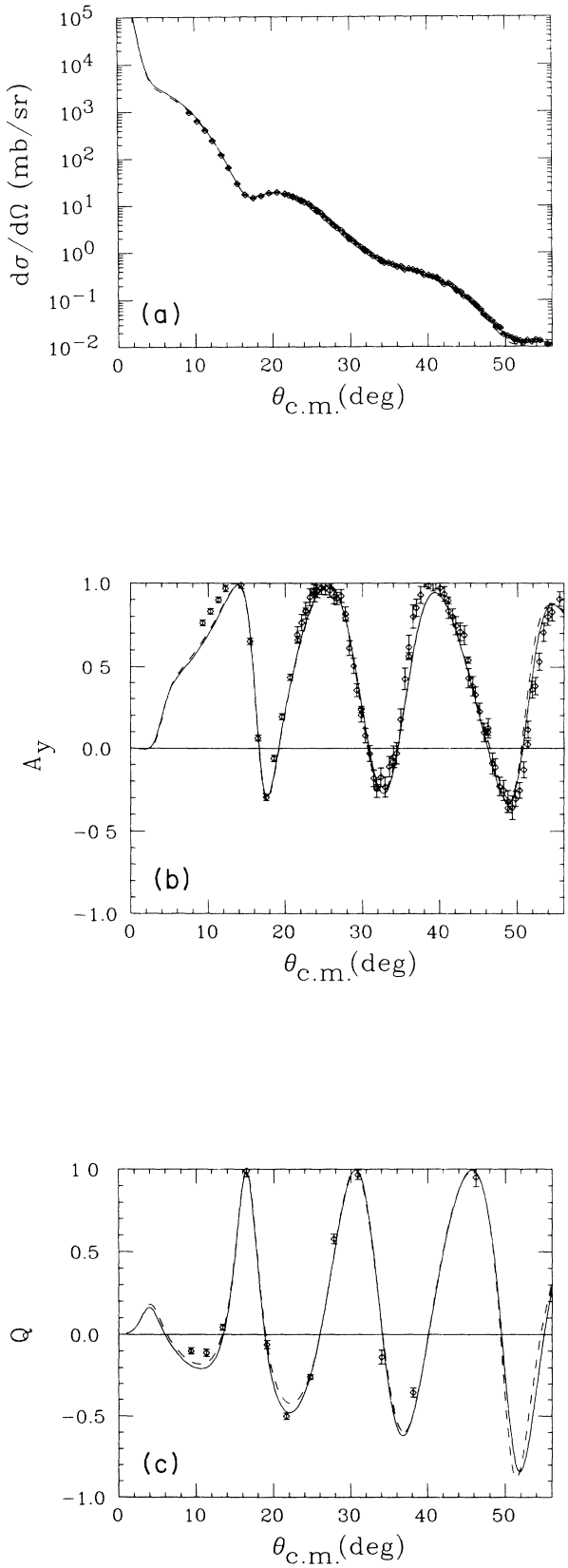

FIG. 12. The same as Fig. 11 except the proton energy is 200 MeV and the data are from Ref. 24.

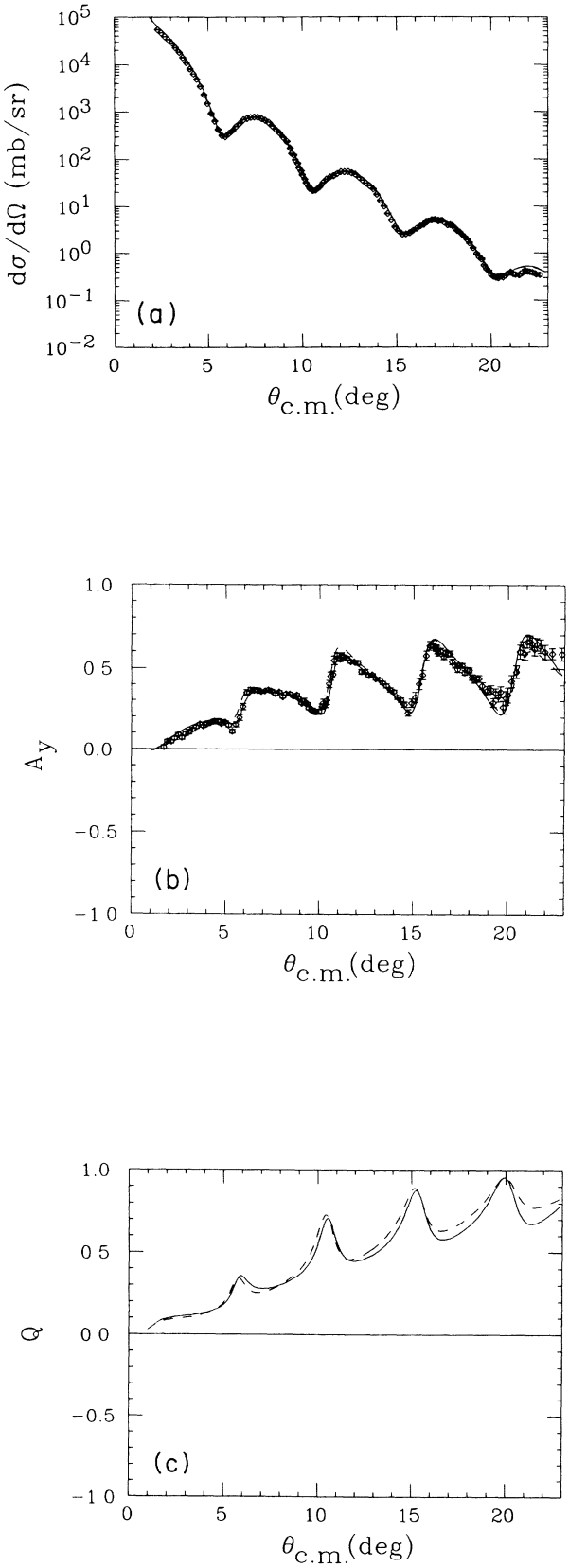

FIG. 13. The same as Fig. 11 except the target is ^{90}Zr and the proton energy is 800 MeV. The data are from Ref. 34.

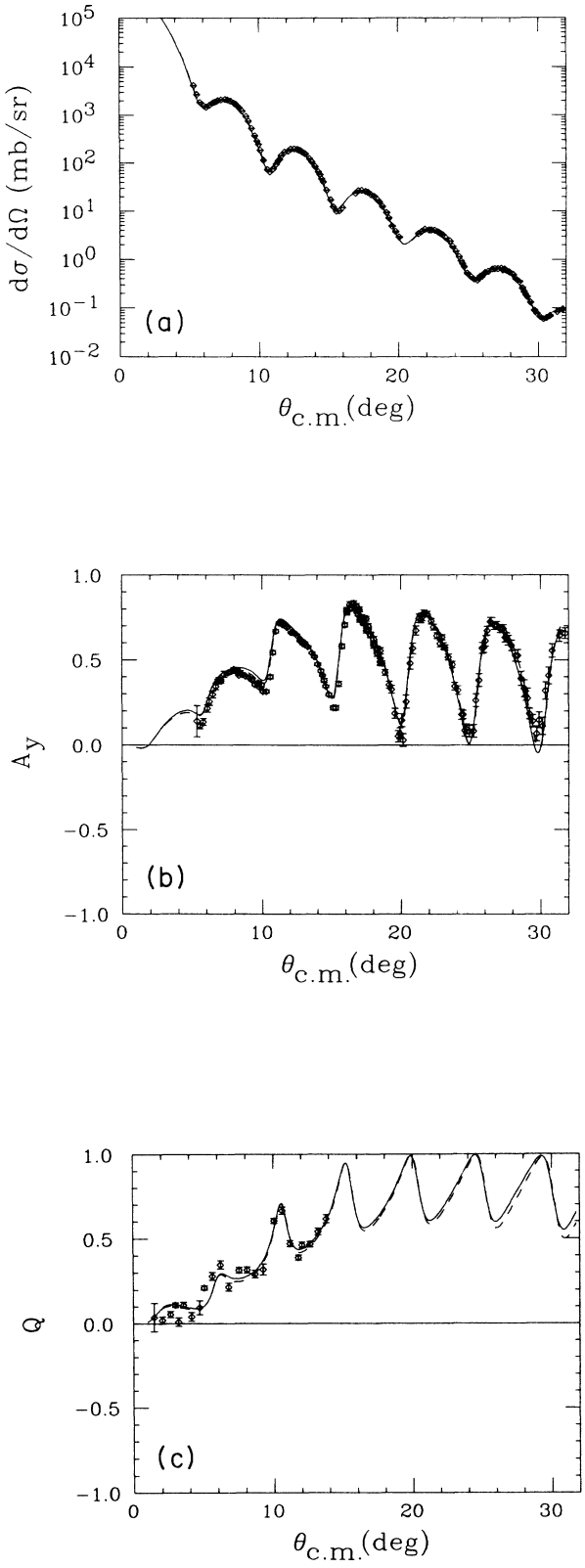

FIG. 14. The same as Fig. 11 except the target is ^{208}Pb and the proton energy is 497.5 MeV. The data are from Refs. 26 and 28.

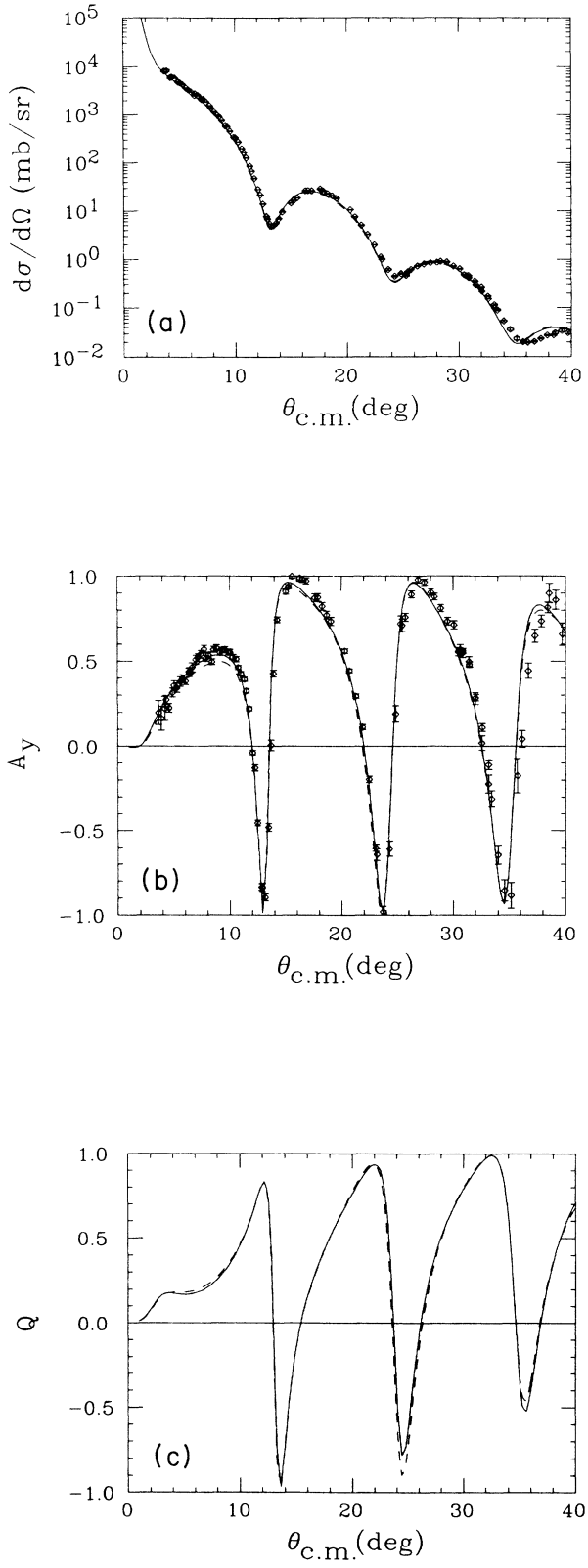

FIG. 15. Predicted elastic scattering observables at 362 MeV for $p + ^{40}$Ca calculated using the parameters of fits 1 (solid line) and 2 (dashed line). The data were not part of the global data set. The experimental data are from Ref. 39.

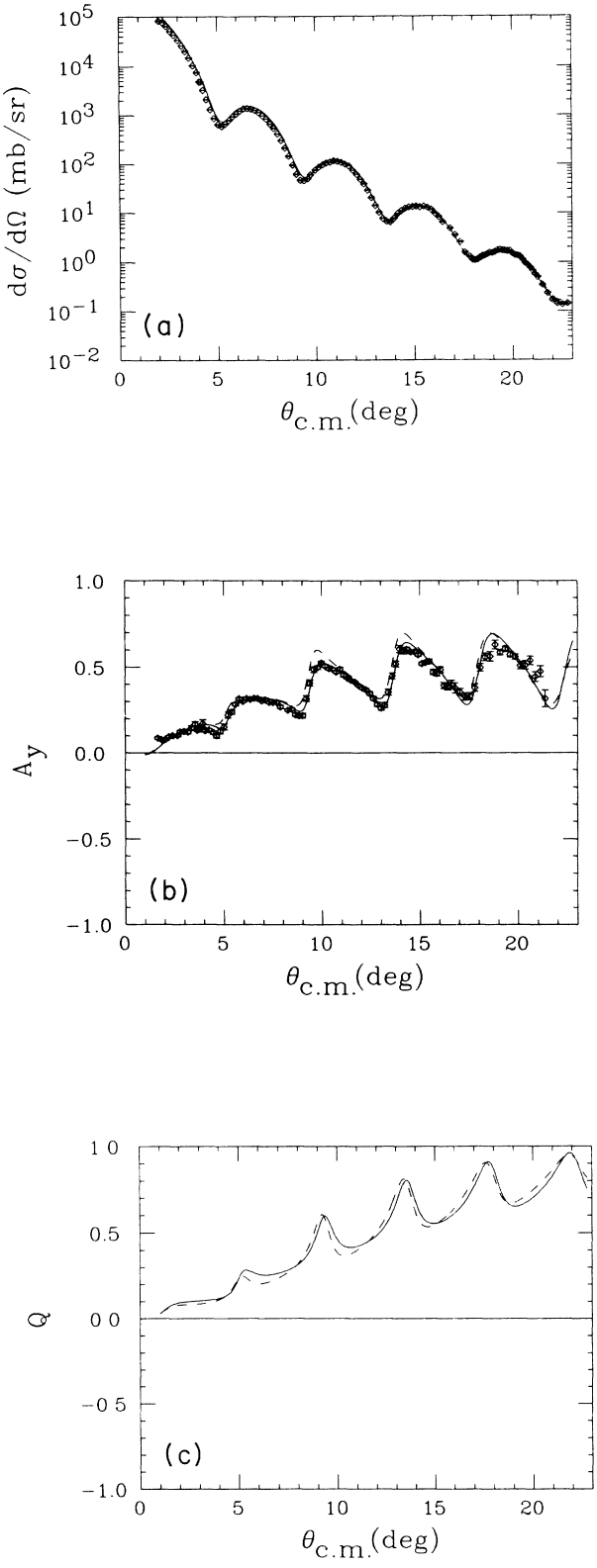

FIG. 16. Predicted elastic scattering observables at 795.5 MeV for $p + {}^{124}\mathrm{Sn}$; data with this value of A were not part of the global data set. The parameters of fits 1 (solid line) and 2 (dashed line) are used. The experimental data are from Ref. 40.

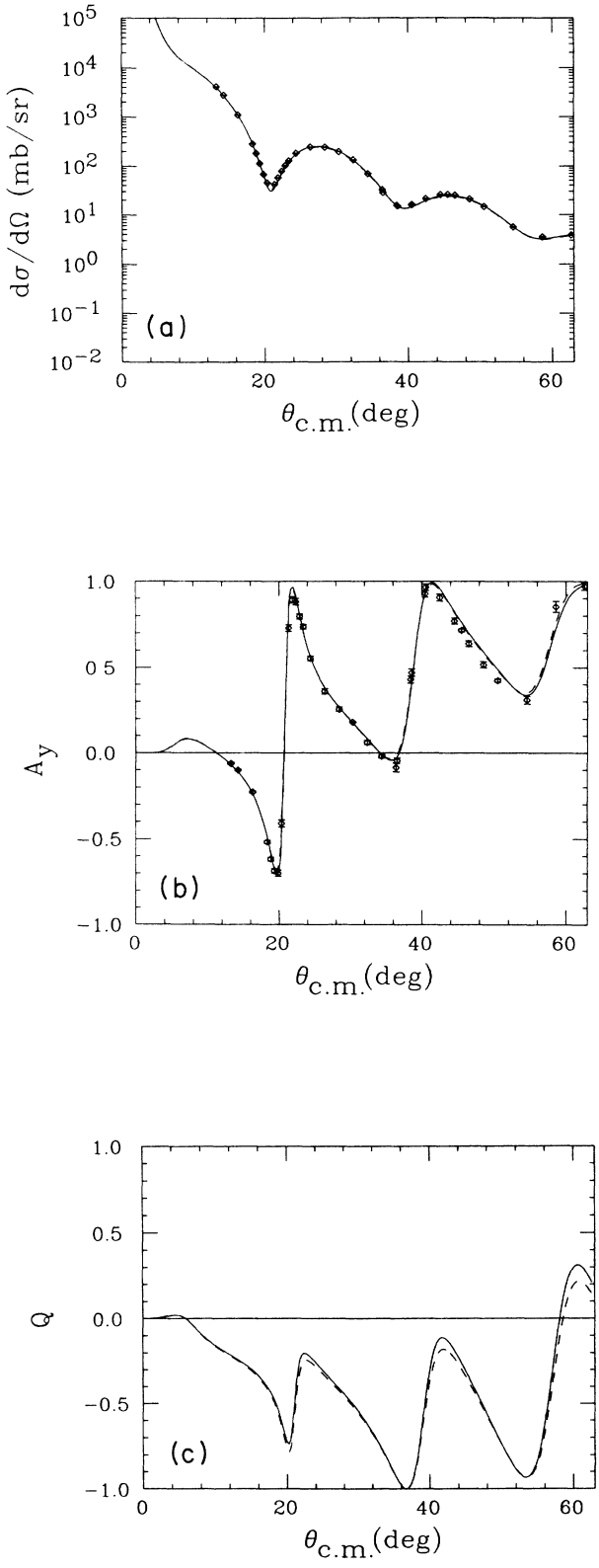

FIG. 17. Predicted elastic scattering observables at 65 MeV for the odd-A target $p + {}^{89}\mathrm{Y}$, calculated using the parameters of fits 1 (solid line) and 2 (dashed line). The experimental data are from Ref. 21.

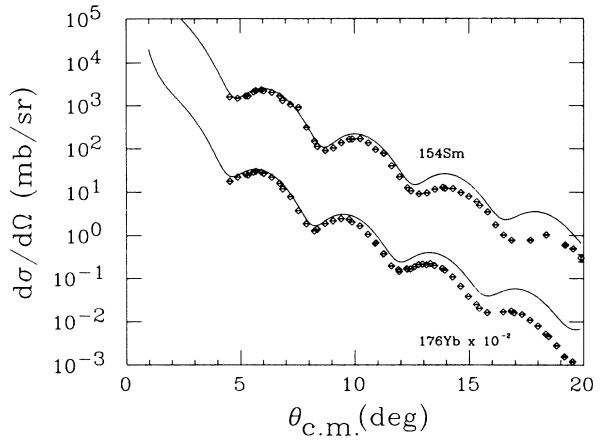

FIG. 18. Predicted elastic scattering cross sections for ^{154}Sm and ^{176}Yb at 800 MeV using the parameters of fit 1. Fit 2 gives essentially the same results. The data are from Ref. 41.

the lowest energy included in the fit. The results of calculations using the predicted optical potentials are shown in Fig. 19 along with data. Fits 1 and 2 give qualitatively the same results as is shown in the figure, although neither give the normalization correctly. For both cases the calculated cross section exhibits a slightly deeper first minimum that the data, although the calculated A_y reproduces data fairly well. The results of a similar extrapolation for ^{208}Pb at 40 MeV are shown in Fig. 20, and in this case the results from both fits are somewhat more acceptable over the angular range included in the data set. An extrapolation in E and interpolation in A can be tested, considering the cross section data for the calcium isotopes[40,42,44,48] Ca at 45 MeV, unfortunately spin observables are not available for most of these targets but, as shown in Fig. 21, the cross sections are quite well reproduced out to 90 deg. In order to illustrate the problems which can occur if the extrapolation is too large, we show the results of an extrapolation to 21 MeV. The results, shown in Fig. 22, retain some of the features of the data, but clearly are not a quality fit. It is not possible to test the extrapolation to higher energies, as data do not exist except for light nuclei. We have no reason to expect the extrapolation to higher energies within the A range included in the fit would be better than that of the extrapolation to lower energies.

The results of an extrapolation in A to ^{16}O prove to be completely terrible and illustrate the danger of using the parameters outside the range of the fit. Our advice regarding extrapolation in A is do not do it. We anticipate that global parametrizations for light nuclei will be available in the near future; single-energy fits or fits for single A's can be obtained from the authors.

In order to compare with nonrelativistic treatments we consider the effective central and spin-orbit potentials defined in Eqs. (4) and (6). These effective central and spin-orbit potentials for $p+^{40}$Ca and $p+^{208}$Pb are shown in Figs. 23–26 for the same cases considered in Figs.

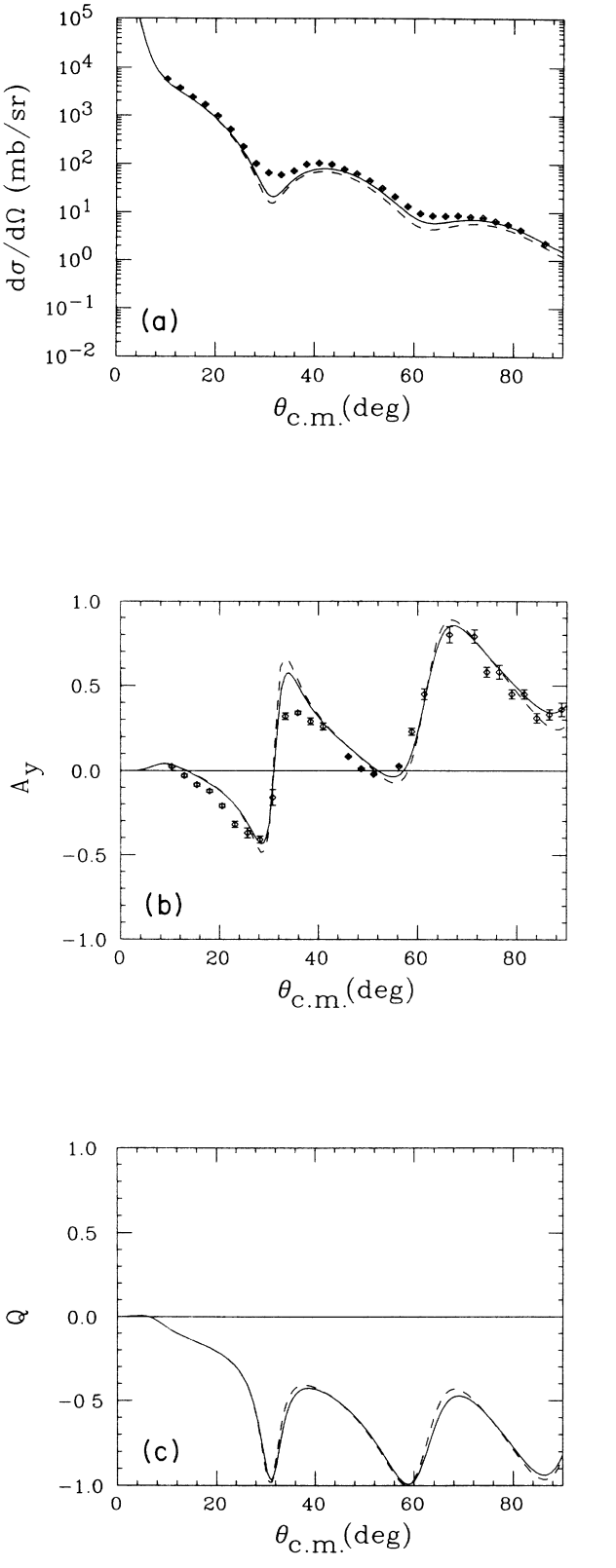

FIG. 19. Elastic scattering observables at 40 MeV for $p+^{40}$Ca, calculated using extrapolation of the parameters of fit 1 (solid line) and fit 2 (dashed line). The experimental data are from Refs. 42 and 43.

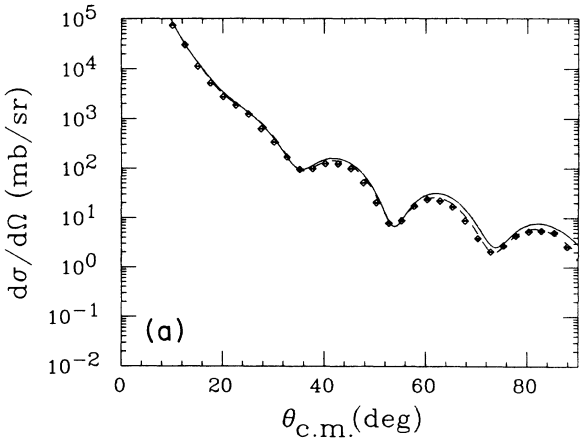

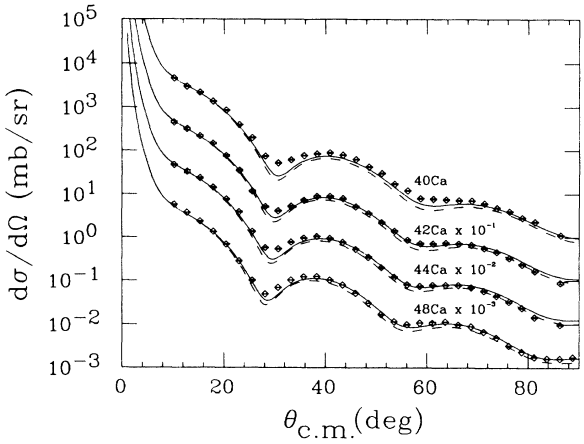

FIG. 21. The same as Fig. 19 except that the incident proton energy is 45 MeV and the targets are ^{40,42,44,48}Ca. The experimental data are from Ref. 42.

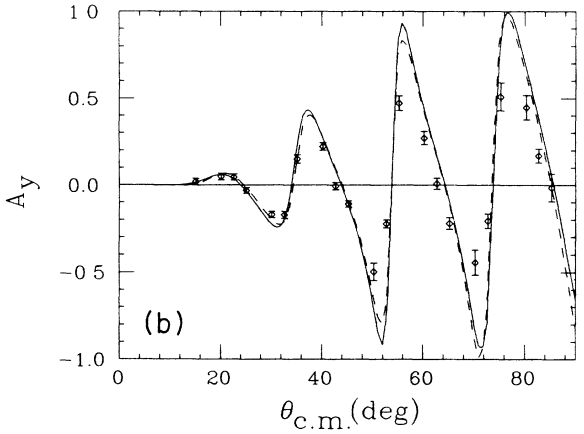

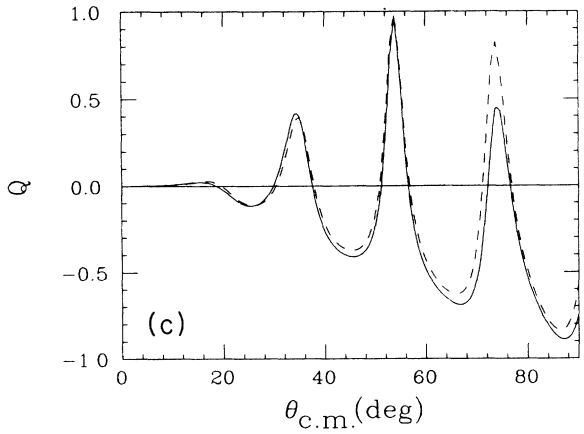

FIG. 20. The same as Fig. 19 except for a 40 MeV proton incident on a ^{208}Pb target. The experimental data are from Refs. 43 and 44.

1–4. It is interesting to note that the imaginary central optical potential for $p+^{40}$Ca shown in Fig. 23 has roughly the same value (between -36 and -40 MeV) at the origin for both energies. The lower energy has a longer range, the rms radii are 3.56 and 3.53 fm for the 497.5 MeV fit 1 and fit 2 cases, and 4.48 and 4.66 fm for fit 1 and fit 2 at 65 MeV. The real central optical potentials are, of course, very different. At 497.5 MeV we observe a pocket of attraction at the nuclear surface, while the 65 MeV potentials are attractive throughout and have a longer range. The real spin-orbit potentials for $p+^{40}$Ca shown in Fig. 24 exhibit a strong energy dependence, with the 65 MeV fits being almost a factor of 3 larger at the maximum, which occurs at about 3.5 fm for both energies. The imaginary spin-orbit potentials all have roughly the same value at their respective maxima; however, the position of the maxima shifts to larger radius as the energy increases. As is shown in Fig. 25, the imaginary central potentials for $p+^{208}$Pb exhibit the same behavior as $p+^{40}$Ca at the origin; all fits at both energies have a value very close to -40 MeV, with the range of the potential being larger at 65 MeV. The two rms radii at 65 MeV are 6.99 fm (fit 1) and 7.04 fm (fit 2) as compared to 5.61 fm (fit 1) and 5.57 fm (fit 2) for 497.5 MeV. Again the 497.5 MeV real central potentials exhibit a pocket of attraction at the nuclear surface and, at 65 MeV, the real central potentials clearly show a nonstandard shape. The real spin-orbit potentials for $p+^{208}$Pb, shown in Fig. 26, are smaller than those for $p+^{40}$Ca. The values at the maximum for 65 MeV are again a factor of 3 larger than those at 497.5 MeV. In contrast to $p+^{40}$Ca, the value of radius at which the maxima in the spin orbit occurs is about the same for both real and imaginary parts of the spin-orbit potential at both energies. One of the features of these analyses is that they predict a more general geometry for the effective central potential than is commonly used in most nonrelativistic calculations. This departure from WS shapes is a feature of the Dirac approach, and is due to the presence of nonlinear terms in the central potential.

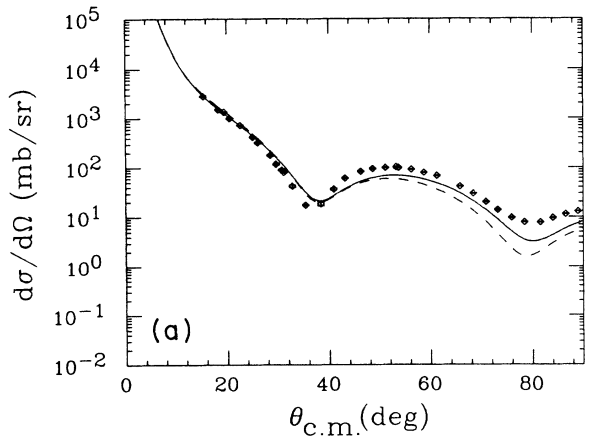

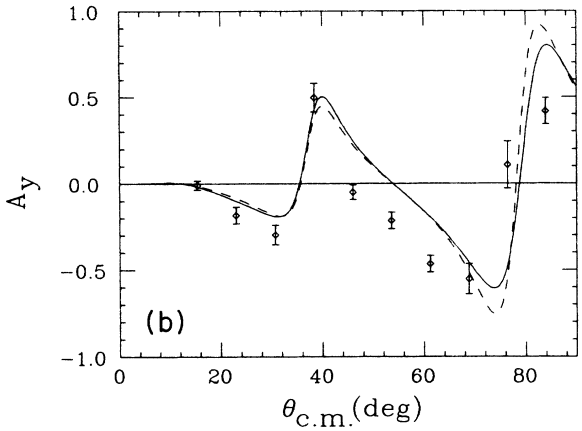

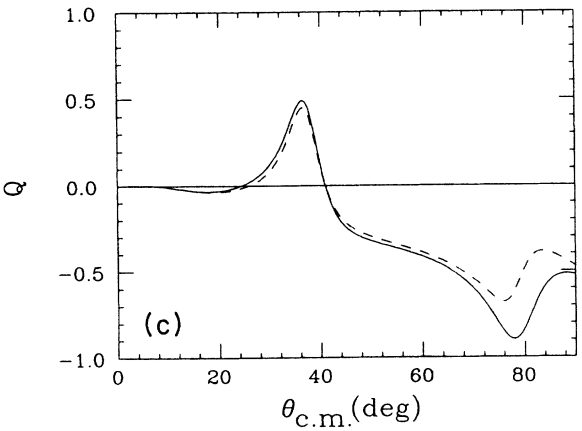

FIG. 22. The same as Fig. 19 except for $p + {}^{40}$Ca at 21 MeV. The experimental data are from Ref. 45.

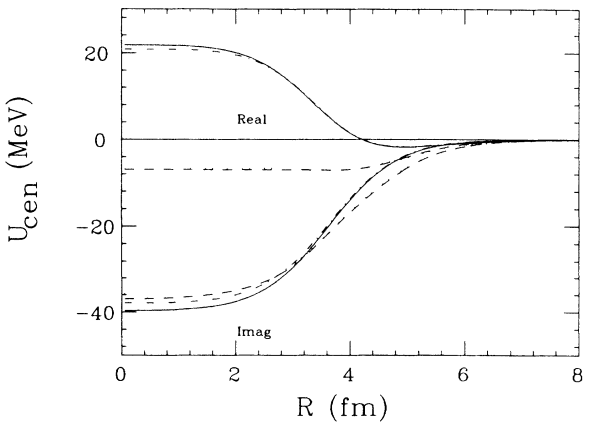

FIG. 23. The Schrödinger equivalent effective central potentials for $p + {}^{40}$Ca for the same cases in Figs. 1 and 2. The solid line is fit 1 at 497.5 MeV, the dashed line is fit 1 at 65 MeV, the dashed-dotted line is fit 2 at 497.5 MeV, and the dotted line is fit 2 at 65 MeV.

In order to further illustrate the behavior of the global potentials, we show in Figs. 27 and 28 the variation of the volume integral per nucleon of the real and imaginary effective central and spin-orbit potentials. The solid lines representing ^{40}Ca agree very well with the dashed lines which give the results for ^{208}Pb. We note that the real volume integral for $p + {}^{40}$Ca changes sign at a higher energy than that of $p + {}^{208}$Pb for both fits, even though the values for $p + {}^{208}$Pb are greater than those of $p + {}^{40}$Ca at lower energies. A similar crossing occurs for the imaginary volume integrals, which increase rapidly with energy above 100 MeV. The volume integrals are of course constrained to vary smoothly with the incident proton kinetic energy, but they also show very small variation with mass number; they agree to within 10% at a fixed energy. In Figs. 29 and 30 we show the energy dependence of the volume integral per nucleon of the real and imaginary scalar and vector potentials and we observe that the real

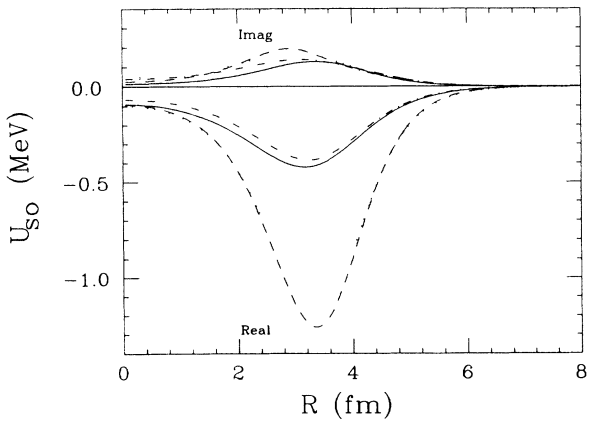

FIG. 24. The same as Fig. 23 except for the Schrödinger equivalent effective spin-orbit potentials.

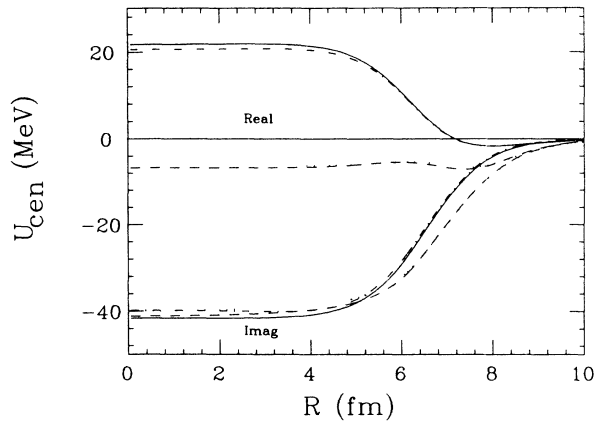

FIG. 25. The Schrödinger equivalent effective central potentials for $p + {}^{208}$Pb for the same cases given in Figs. 3 and 4. The curves are identified as in Fig. 23.

values for Ca and Pb for fit 1 tend to converge at higher energies; however, the behavior of the imaginary volume integrals for fit 2 exhibits a marked energy dependence due to the form chosen for the energy dependence of the surface term. The energy dependence of the surface term in fit 1 is chosen to "turn off" as the energy increases. We show the values for the real rms radii of these potentials in Figs. 31 and 32 and we note in particular the strong energy dependence in the imaginary rms radii, especially for the potentials of fit 2.

Finally we show our results for the predicted reaction cross sections. These data were not included in the data set. As can be seen from Fig. 33, the predicted reaction cross sections from both fits are in reasonable agreement with experiment.

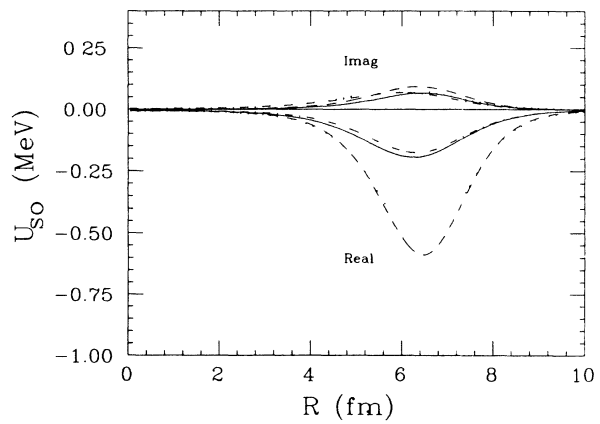

FIG. 26. The same as Fig. 25 except for the Schrödinger equivalent effective spin-orbit potentials.

IV. A TEST OF RESULTS USING A COUPLED CHANNEL DIRAC TREATMENT OF INELASTIC SCATTERING

In this section we present a test of the effects of the different global parametrizations on a simple reaction calculation. We consider inelastic proton-nucleus scattering within the framework of the collective model. The treatment is relativistic in that the calculations are done using a Dirac coupled channel (CC) approach; see Refs. 5–7. In order to test the effects of using different direct potentials we consider the following procedure. First, excellent representations of the 3^- inelastic observables for ^{40}Ca at 500 MeV have been obtained within a generalization of the nonrelativistic collective model appropriate for use in a Dirac equation.[7] In this model the direct potential is determined by fitting the elastic data, and the Lorentz scalar and vector transition potentials for a state of multipolarity λ are simply written

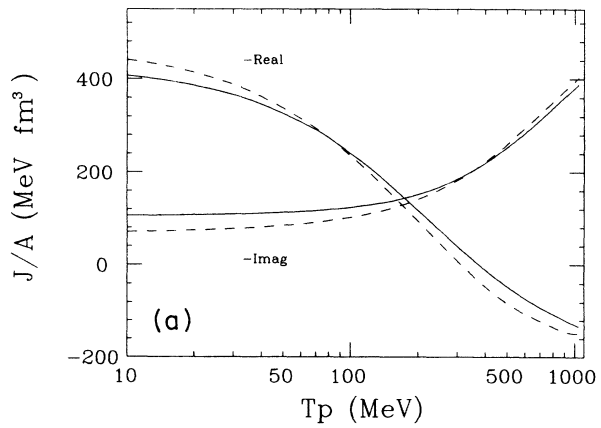

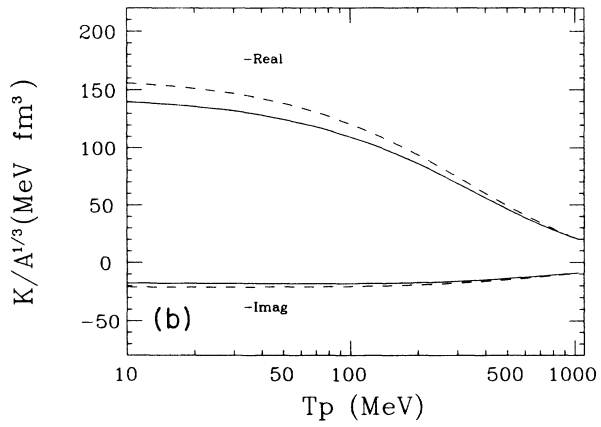

FIG. 27. The volume integral per nucleon of the effective central potential J/A, and the volume integral of the effective spin-orbit potential divided by $A^{1/3}$, $K/A^{1/3}$, for fit 1 parameters. The solid line shows the results for $p + {}^{40}$Ca and the dashed line shows the results for $p + {}^{208}$Pb.

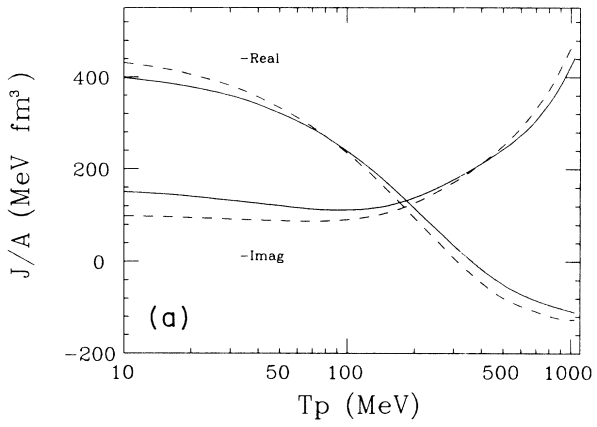

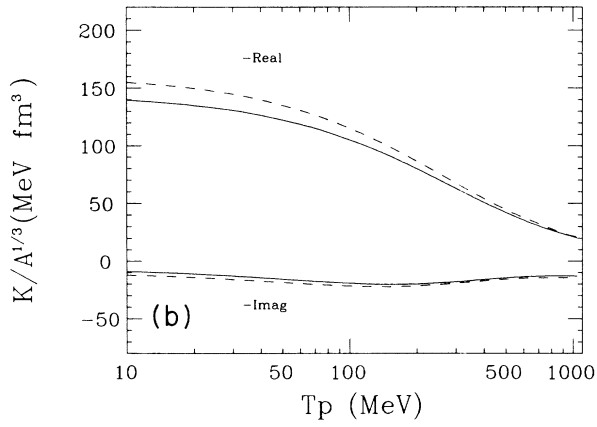

FIG. 28. The same as Fig. 27 except that the parameters of fit 2 are used.

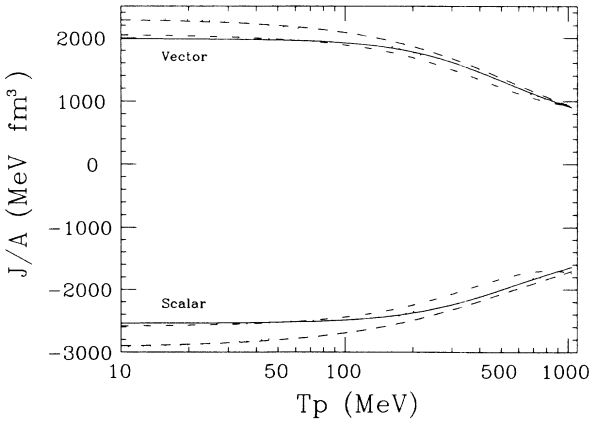

FIG. 29. The volume integral per nucleon for real scalar and vector optical potentials as a function of incident proton lab energy for $p+^{40}$Ca and $p+^{208}$Pb. The parameters of fits 1 and 2 are used. The solid line shows the fit 1 $p+^{40}$Ca results, the dashed line shows the fit 1 $p+^{208}$Pb results, the dash-dotted line shows the fit 2 $p+^{40}$Ca results, and the dotted line shows the fit 2 $p+^{208}$Pb results.

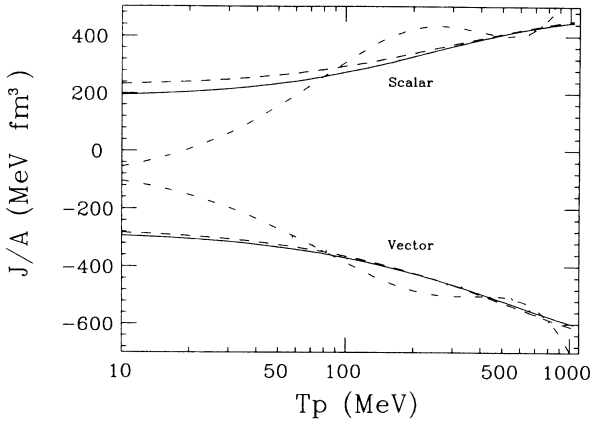

FIG. 30. The same as Fig. 29 except for the imaginary scalar and vector potentials.

$$S_T=\frac{\delta_\lambda}{\sqrt{2\lambda+1}}\frac{dS}{dr}Y_{\lambda\mu}(\theta\phi)\ , \tag{23}$$

and

$$V_T=\frac{\delta_\lambda}{\sqrt{2\lambda+1}}\frac{dV}{dr}Y_{\lambda\mu}(\theta\phi)\ , \tag{24}$$

where the deformation lengths are determined from fitting the inelastic data using a Dirac CC approach to calculate the observables. In a consistent CC calculation the elastic and inelastic data are searched together. Here, in order to see the effects of using different direct (elastic) potentials we do no further searching on the elastic parameters of fits 1 and 2. Two calculations are of interest. First, with a given set of deformation lengths what are the differences in the inelastic observables, and second, what is the difference in the extracted deformation lengths when the inelastic data are fit using these different

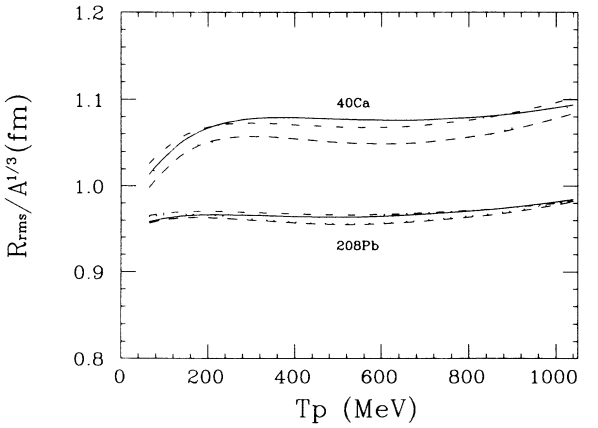

FIG. 31. The root-mean-square radii of the real scalar and vector potentials for the potentials shown in Fig. 29. The solid line shows the fit 1 scalar results, the dashed line shows the fit 1 vector results, the dash-dotted line shows the fit 2 scalar results, and the dotted line shows the fit 2 vector results.

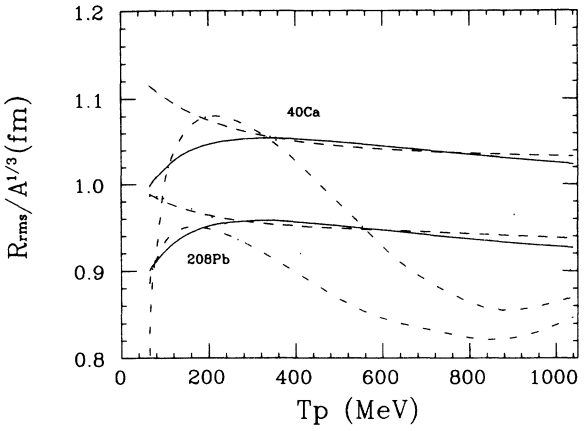

FIG. 32. The same as Fig. 31 except for the potentials shown in Fig. 30.

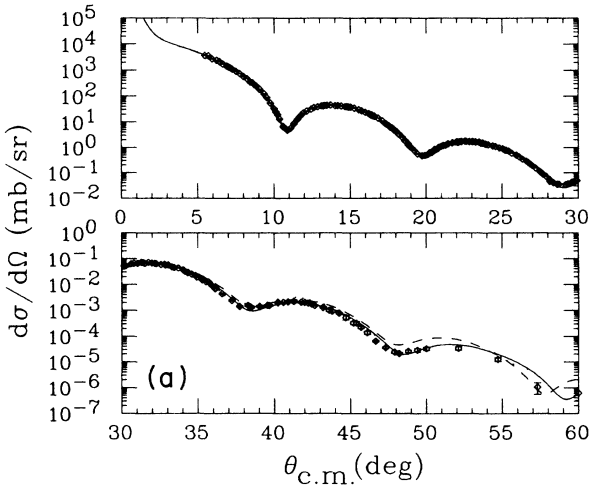

potentials. In the first case we find that the inelastic observables are essentially uneffected by the choice of which of the two global potentials is used. For the second test, we find less than 1% difference in the extracted deformation lengths from the two fits, and as shown in Figs. 34 and 35, the representation of the elastic and inelastic data is quite good over the angular range considered. These calculations were meant to give some indication of the stability of the global potentials when used in a reaction calculation. Of course the situation can change when other reactions are considered.

V. SUMMARY AND CONCLUSIONS

We have obtained two global parametrizations of the scalar and vector Dirac optical potentials. The parameters are functions of both energy and target mass number.

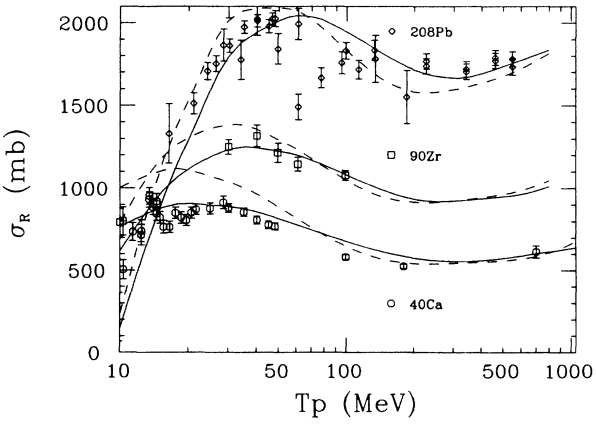

FIG. 33. Predicted total reaction cross sections for ^{40}Ca, ^{90}Zr, and ^{208}Pb as a function of incident proton lab energy using the parameters of fits 1 (solid line) and 2 (dashed line). The data are from Ref. 46.

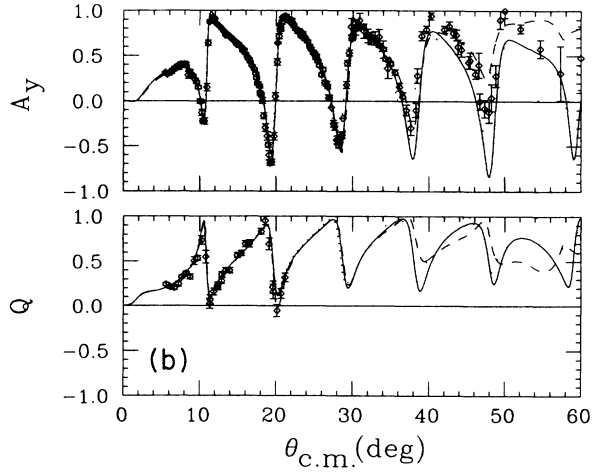

FIG. 34. Calculated elastic observables at 497.5 MeV with the 3^- state coupled for fits 1 (solid line) and 2 (dashed line). The dotted line is the calculation using fit 1 without the 3^- state. The data are from Refs. 26 and 27.

The characteristics of the two fits have been investigated, and it is observed that they are quite similar except for the treatment of the surface terms. We have shown that both fits reproduced elastic proton-nucleus observables quite well. We have also investigated the characteristics of the global fits with respect to interpolation and extrapolation in both E and A. In Sec. IV we discussed the differences which occur in a reaction calculation using either fit 1 or fit 2. The differences were not large.

It is important to remember that global optical potentials given in this paper have their limitations:

(i) They are applicable only to spherical nuclei with

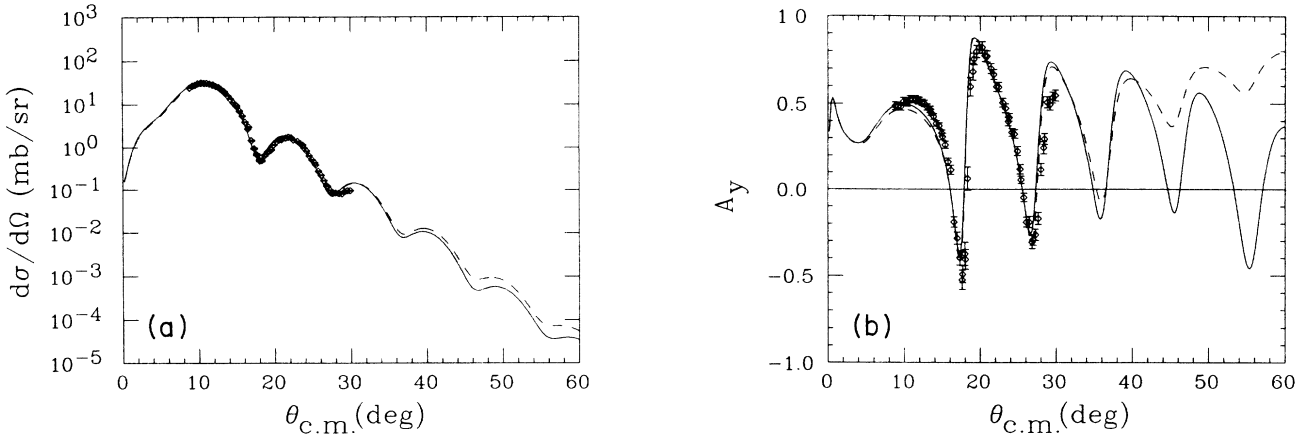

FIG. 35. Calculated inelastic observables at 497.5 MeV for the 3^- state of $p+^{40}$Ca using the parameters of fits 1 (solid line) and 2 (dashed line). The data are from Refs. 47 and 48.

mass numbers $40 \leq A \leq 208$.

(ii) Interpolation in E and A works quite well, extrapolation in E and A is however, not recommended.

(iii) The data set did not include data beyond $90°_{\text{c.m.}}$ or 3 fm^{-1}; thus it is not expected that this model can produce good agreement with data beyond that range.

A program written to produce scalar and vector optical potentials from fits 1 and 2 presented here, tabulated as a function of radius, is available from the authors.[49]

ACKNOWLEDGMENTS

We thank S. Shim for performing the calculation discussed in Sec. IV, and John Davis for helpful conversations. This work was supported in part by the National Science Foundation, under Grant Nos. PHY-8600702 and PHY-8822550, the Natural Sciences and Engineering Research Council of Canada, and a grant from the Ohio Supercomputer Center.

*Present address: Department of Physics, The Ohio State University, Columbus, OH 43210.

[1]H. S. Sherif, R. I. Sawafta, and E. D. Cooper, Nucl. Phys. **A449**, 708 (1986).

[2]J. I. Johansson, E. D. Cooper, and H. S. Sherif, Nucl. Phys. **A476**, 663 (1988).

[3]K. H. Hicks and J. Lisantti, Nucl. Phys. **A484**, 432 (1988).

[4]B. C. Clark, S. Hama, E. Sugarbaker, M. A. Franey, R. L. Mercer, L. Ray, G. W. Hoffmann, and B. D. Serot, Phys. Rev. C **30**, 314 (1984).

[5]J. Raynal, in *Workshop on Applied Theory and Nuclear Model Calculations for Nuclear Technology Applications* (IUCP, Trieste, 1988); in *Proceedings of the Sixth International Symposium on Polarization Phenomena in Nuclear Physics, Osaka, 1985,* edited by M. Kondo, S. Kobayashi, M. Tanifuji, T. Yamazaki, K.-I. Kubo, and N. Onishi, Supplement to the Journal of the Physical Society of Japan, Vol. 55, 1986, Physical Society of Japan, p. 922.

[6]R. D. Swiniarski, D. L. Pham, and J. Raynal, Phys. Lett. B **213**, 247 (1988). See also, J. Raynal, H. S. Sherif, A. M. Kobos, E. D. Cooper, and J. I. Johansson, Phys. Lett. B **218**, 403 (1989).

[7]S. Shim, B. C. Clark, S. Hama, R. Mercer, E. D. Cooper, R. Ray, and Hoffmann, Phys. Rev. C **44**, 111 (1988).

[8]E. D. Cooper, B. C. Clark, R. Kozack, S. Shim, S. Hama, J. I. Johansson, H. S. Sherif, R. L. Mercer, and B. D. Serot, Phys. Rev. C **36**, 2170 (1987).

[9]E. D. Cooper, B. C. Clark, S. Hama, and R. L. Mercer, Phys. Lett. B **206**, 588 (1988); **220**, 658(E) (1989).

[10]R. Kozack and D. G. Madland, Phys. Rev. C **39**, 1461 (1989).

[11]H. O. Meyer, P. Schwandt, R. Abegg, C. A. Miller, K. P. Jackson, S. Yen, G. Gaillard, M. Hugi, R. Helmer, D. Frekers, and A. Saxena, Phys. Rev. C **37**, 544 (1989).

[12]E. D. Cooper and O. V. Maxwell, Nucl. Phys. **A493**, 468 (1989). Please note a typographical error in Table 1 of this paper. The entry for R in the first column should read 3.559 570, not 3.538 693.

[13]B. C. Clark, S. Hama, and R. L. Mercer, in *Proceedings of the Workshop on the Interaction Between Medium Energy Nucleons in Nuclei* (Indiana University Cyclotron Facility, Bloomington, Indiana), AIP Conf. Proc. No. 97, edited by H. O. Meyer (AIP, New York, 1982), p. 260. See also, B. C. Clark, in *Proceedings of the Workshop on Relativistic Dynamics and Quark-Nuclear Physics,* edited by M. B. Johnson and A. Picklesimer (Wiley, New York, 1986), p. 302; in *Proceedings of the International Symposium on Medium Energy Nucleon and Antinucleon Scattering, Bad Honnef, West Germany,* edited by H. V. von Geramb (Springer-Verlag, Berlin, 1985), p. 391; in *Proceedings of the Bates Users Theory Group Workshop on Relativistic Effects and Hadronic Structure,*

MIT, 1985, edited by J. Dubach and F. Gross (MIT Press, Cambridge, MA, 1985), p. 101.

[14]B. C. Clark, R. L. Mercer, and P. Schwandt, Phys. Lett. **122B**, 211 (1983).

[15]A. M. Kobos, E. D. Cooper, J. I. Johansson, and H. S. Sherif, Nucl. Phys. **A445**, 605 (1985).

[16]L. G. Arnold, B. C. Clark, R. L. Mercer, and P. Schwandt, Phys. Rev. C **23**, 1949 (1981).

[17]R. L. Schutt, R. E. Shamu, P. W. Lisowski, M. S. Moone, and G. L. Morgan, Phys. Lett. B **203**, 22 (1988).

[18]E. D. Cooper, Ph.D. thesis, University of Alberta, 1981.

[19]R. L. Mercer, Ph.D. thesis, University of Illinois, 1972.

[20]E. D. Cooper and B. K. Jennings, Nucl. Phys. A **483**, 601 (1988).

[21]H. Sakaguchi, M. Nakamura, K. Hatanaka, A. Goto, T. Noro, F. Ohtani, H. Sakamoto, H. Ogawa, and S. Kobayashi, Phys. Rev. C **26**, 944 (1982).

[22]P. Schwandt, H. O. Meyer, W. W. Jacobs, A. D. Bacher, S. E. Vigdor, M. D. Kaitchuck, and T. R. Donoghue, Phys. Rev. C **26**, 55 (1982).

[23]A. Nadasen, P. Schwandt, P. P. Singh, W. W. Jacobs, A. D. Bacher, P. T. Debevec, M. D. Kaitchuck, and J. T. Meek, Phys. Rev. C **23**, 1023 (1981).

[24]E. Stephenson, *Antinucleon- and Nucleon-Nucleus Interactions,* edited by G. E. Walker, C. D. Goodman, and C. Olmer (Plenum, New York, 1985), p. 299.

[25]D. A. Hutcheon, J. M. Cameron, R. P. Liljestrand, P. Kitching, C. A. Miller, W. J. McDonald, D. M. Sheppard, W. C. Olsen, G. C. Neilson, H. S. Sherif, R. N. MacDonald, G. M. Stinson, D. K. McDaniels, J. R. Tinsley, L. W. Swenson, P. Schwandt, C. E. Stronach, and L. Ray, in *Proceedings of the Fifth International Symposium on Polarization Phenomena in Nuclear Physics, Santa Fe, 1980,* AIP Conf. Proc. No. 69, edited by G. G. Ohlsen, R. E. Brown, N. Jarmie, W. W. McNaughton, and G. M. Hale (AIP, New York, 1981), p. 454.

[26]G. W. Hoffmann, L. Ray, M. L. Barlett, R. Fergerson, J. McGill, E. C. Milner, K. K. Seth, D. Barlow, M. Bosko, S. Iverson, M. Kaletka, A. Saha, and D. Smith, Phys. Rev. Lett. **47**, 1436 (1981).

[27]A. Rahbar, B. Aas, E. Bleszynski, M. Bleszynski, M. Haji-Saeid, G. J. Igo, F. Irom, G. Pauletta, A. T. M. Wang, J. B. McClelland, J. F. Amann, T. A. Carey, W. D. Cornelius, M. Barlett, G. W. Hoffmann, C. Glashausser, S. Nanda, and M. M. Gazzaly, Phys. Rev. Lett. **47**, 1811 (1981).

[28]B. Aas, E. Bleszynski, M. Bleszynski, M. Haji-Saeid, G. Igo, F. Irom, G. Pauletta, A. Rahbar, A. Wang, J. F. Amann, T. A. Carey, W. Cornelius, J. B. McClelland, M. Barlett, G. Hoffmann, M. Gazzaly, C. Glashausser, and S. Nanda, Bull. Am. Phys. Soc. **26**, 1125 (1981).

[29]Centre d'Etudes Nucléaires de Saclay Report Dph-N/ME/78-1, 1978.

[30]G. Igo, G. S. Adams, T. S. Bauer, G. Pauletta, C. A. Whitten Jr., A. Wreikat, G. W. Hoffmann, G. S. Blanpied, W. R. Coker, C. Harvey, R. P. Liljestrand, L. Ray, J. E. Spencer, H. A. Thiessen, C. Glashausser, N. M. Huntz, M. A. Oothoudt, H. Nann, K. K. Seth, B. E. Wood, D. K. McDaniels, and M. Gasszly, Phys. Lett. **81B**, 151 (1979).

[31]E. Bleszynski, M. Bleszynski, S. Hajisaeid, G. J. Igo, F. Irom, J. B. McClelland, G. Pauletta, A. Rahbar, A. T. M. Wang, C. A. Witten, Jr., G. Adams, M. Barlett, G. W. Hoffmann, J. A. McGill, R. Boudrie, and G. Kyle, Phys. Rev. C **25**, 2563 (1982).

[32]R. W. Fergerson, M. L. Barlett, G. W. Hoffmann, J. A. Marshall, E. C. Milmer, G. Pauletta, L. Ray, J. F. Amann, K. W. Jones, J. B. McClelland, M. Gazzaly, and G. J. Igo, Phys. Rev. C **33**, 239 (1986).

[33]G. D. Alkhazov, T. Bauer, R. Beurtey, A. Boudard, G. Bruge, A. Chaumeaux, P. Couvert, G. Cvijanovich, H. H. Duhm, J. M. Fontaine, D. Garreta, A. V. Kulikov, D. Legrand, J. C. Lugol, J. Saudinos, J. Thirion, and A. A. Vorobyov, Nucl. Phys. **A274**, 443 (1976).

[34]L. Ray, G. W. Hoffmann, G. S. Blanpied, W. R. Coker, and R. P. Liljestrand, Phys. Rev. C **18**, 1756 (1978).

[35]D. A. Hutcheon, J. M. Cameron, R. P. Liljestrand, P. Kitching, C. A. Miller, W. J. McDonald, D. M. Sheppard, W. C. Olsen, G. C. Neilson, H. S. Sherif, D. K. McDaniels, J. R. Tinsley, L. W. Swenson, P. Schwandt, C. E. Stronach, and L. Ray, Phys. Rev. Lett. **47**, 315 (1981).

[36]G. W. Hoffmann, L. Ray, M. Barlett, W. R. Coker, J. McGill, G. S. Adams, G. J. Igo, F. Irom, A. T. M. Wang, C. A. Whitten, Jr., R. L. Boudrie, J. F. Amann, C. Glashausser, N. M. Hintz, G. S. Kyle, and G. S. Blanpied, Phys. Rev. C **24**, 541 (1981).

[37]B. C. Clark, S. Hama, R. L. Mercer, L. Ray, and B. D. Serot, Phys. Rev. Lett. **50**, 1644 (1983); B. C. Clark, S. Hama, R. L. Mercer, L. Ray, G. W. Hoffmann, and B. D. Serot, Phys. Rev. C **28**, 1421 (1983).

[38]D. P. Murdock and C. J. Horowitz, Phys. Rev. C **35**, 1442 (1987).

[39]D. Frekers, S. S. M. Wong, R. E. Azuma, T. E. Drake, J. D. King, L. Buchmann, R. Schubank, R. Abegg, K. P. Jackson, C. A. Miller, S. Yen, W. P. Alford, R. L. Helmer, C. Broude, S. Mattsson, and E. Rost, Phys. Rev. C **35**, 2236 (1987).

[40]G. W. Hoffmann, G. S. Blanpied, W. R. Coker, R. P. Liljestrand, L. Ray, J. E. Spencer, H. A. Thiessen, N. M. Hintz, M. A. Oothoudt, T. S. Bauer, G. Igo, G. Pauletta, J. Soukup, C. A. Whitten, Jr., H. Nann, K. K. Seth, C. Glashausser, D. K. McDaniels, J. Tinsley, and P. Varghese, Phys. Lett **76B**, 383 (1978).

[41]M. L. Barlett, J. A. McGill, L. Ray, M. M. Barlett, G. W. Hoffmann, N. M. Hintz, G. S. Kyle, M. A. Franey, and G. Blanpied, Phys. Rev. C **22**, 1168 (1980).

[42]R. H. McCamis, T. N. Nasr, J. Birchall, N. E. Davison, W. T. H. van Oers, P. J. T. Verheijen, R. F. Carlson, A. J. Cox, B. C. Clark, E. D. Cooper, S. Hama, and R. L. Mercer, Phys. Rev. C **33**, 1642 (1986).

[43]L. N. Blumberg, E. E. Gross, A. Van der Woude, A. Zucker, and R. H. Bassel, Phys. Rev. **147**, 812 (1966).

[44]M. P. Fricke, E. E. Gross, B. J. Morton, and Z. Zucker, Phys. Rev. **156**, 1207 (1967).

[45]K. H. Bray, K. S. Jayaraman, G. A. Moss, W. T. H. van Oers, D. O. Wells, and Y. I. Wu, Nucl. Phys. **A167**, 57 (1971).

[46]W. Bauhoff, At. Data Nucl. Data Tables **35**, 429 (1986).

[47]K. K. Seth, D. Barlow, A. Saha, R. Soundranayagam, S. Iversen, M. Kaletka, M. Basko, D. Smith, G. W. Hoffmann, M. L. Barlett, R. Fergerson, J. McGill, and E. C. Milner, Phys. Lett. **158B**, 23 (1985).

[48]M. L. Barlett, G. W. Hoffmann, and L. Ray, Phys. Rev. C **35**, 2185 (1987).

[49]To obtain a copy of the FORTRAN program GLOBAL, please contact B. C. Clark, E. D. Cooper, or S. Hama at the Ohio State University. Bitnet addresses BCC @ OHSTPY, COOPER @ OHSTPY, or HAMA @ OHSTPY. Files can be sent directly to those persons having E-MAIL addresses.